



**European Master of Science  
in Nuclear Fusion and Engineering Physics**

## **Theoretical Study for Alfvénic Stability Optimization in the TJ-II Stellarator**

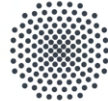
Master Thesis  
presented by

**Luis Carlos Herrera Quesada**

Thesis Supervisor

Jacobo Varela  
Universidad Carlos III de Madrid

June 27th, 2023



Universität Stuttgart





# **Theoretical Study for Alfvénic Stability Optimization in the TJ-II Stellarator**

Master Thesis  
presented by

**Luis Carlos Herrera Quesada**

Thesis Supervisor  
Jacobo Varela  
Universidad Carlos III de Madrid

Erasmus Mundus Program on Nuclear Fusion Science and  
Engineering Physics

June 27th, 2023



# Abstract

Energetic particles (**EP**) in nuclear fusion devices can trigger Alfvén Eigenmodes (**AE**) if the **EP** velocity is similar to the plasma Alfvén velocity. The **AEs** induce **EP** losses during the thermalization process, leading to inefficient plasma heating and damage to the plasma-facing components. Consequently, **AEs** can deteriorate the performance of future nuclear fusion reactors. This thesis is dedicated to studying the **AE** stability in TJ-II device with respect to the NBI operational regime and magnetic trap configuration. The analysis is performed using the linear version of the gyro-fluid code *FAR3d*, that solves the reduced MHD equations for the thermal plasma coupled with moments of the gyro-kinetic equation for the **EPs**, including the effect of the sound wave and the helical couplings. The Alfvén Continuum is computed by the *STELLGAP* code. **AE** stability analysis is performed for the  $n = 7, 11, 15$ ,  $n = 5, 9, 13, 17$ ,  $n = 6, 10, 14$  helical families including EP populations with energies in the range of 10 - 50 keV and **EP** beta from 0.1 to 0.4, identifying the **EP** populations leading to the strongest drive.

Linear simulations for NBI operation shows **AE** stability improvement for deposition at the plasma core if  $\beta_f \leq 0.3$  where unstable  $n/m = 5/3, 6/3$  and  $7/4$  **GAEs** are trigger at higher  $\beta_f$ . Variations in magnetic topology exhibits improve **AE** stability if  $\iota = [1.975, 2.1]$  for  $\beta_f \leq 0.35$ , above which  $n/m = 5/2$  and  $6/3$  **GAEs** are trigger at middle plasma region.

*Keywords:* Alfvén Waves, Resonance, Magnetic Confinement, Stellarator, Neutral Beam Injection, Transport, Magnetohydrodynamics, Magnetic Field



# Contents

<b>1</b>	<b>Introduction</b>	<b>7</b>
1.1	Nuclear Fusion . . . . .	7
1.2	Magnetic Confinement . . . . .	9
1.3	Energetic Particles . . . . .	11
1.4	TJ-II Stellarator . . . . .	12
1.5	Objectives and Structure . . . . .	13
<b>2</b>	<b>Alfvén Eigenmodes Theory</b>	<b>15</b>
2.1	Magnetohydrodynamic Theory . . . . .	15
2.2	Shear Alfvén Waves . . . . .	17
2.3	Alfvén Continuum . . . . .	18
2.4	Alfvén Waves Classification . . . . .	19
2.5	Wave-Particle Energy Transfer . . . . .	20
<b>3</b>	<b>FAR3d and Analysis</b>	<b>23</b>
3.1	Work Scheme . . . . .	23
3.2	Numerical Model . . . . .	25
3.3	Equilibrium Properties . . . . .	27
3.4	Simulation Parameters . . . . .	29
3.4.1	NBI Operational Regime Parameters . . . . .	30
3.4.2	Magnetic Topology Parameters . . . . .	31
3.5	Data Acquisition and Analysis Libraries . . . . .	33
<b>4</b>	<b>Results</b>	<b>37</b>
4.1	NBI Density Profile Variation . . . . .	37
4.1.1	NBI Axis Displacement . . . . .	38
4.1.2	NBI Gradient Variation . . . . .	38
4.2	Magnetic Field Topology Variation . . . . .	51
<b>5</b>	<b>Discussion</b>	<b>57</b>
5.0.1	Optimization of the NBI Operational Regime . . . . .	57
5.0.2	Magnetic Topology Alfvén Eigenmodes Optimization . . . . .	57
<b>6</b>	<b>Conclusions and Future Work</b>	<b>59</b>
<b>A</b>	<b>Nomenclature</b>	<b>65</b>



# List of Figures

1.1	Binding Energy per nucleon vs Mass number (A) [1]. . . . .	8
1.2	Velocity average cross-section for different reactions [2]. . . . .	8
1.3	Charge particle dynamics in the presence of an external magnetic field. . . . .	9
1.4	Plasma confinement concepts for nuclear reactors [3]. . . . .	10
1.5	Nested magnetic closed flux surfaces generated with the VMEC file. . . . .	11
1.6	Two different AE identified in DIII-D discharge [4]. . . . .	12
1.7	TJ-II Stellarator. . . . .	12
1.8	Eagle-view of TJII with schematics of the NBI heating systems [5]. . . . .	13
2.1	Line bending of the magnetic field that represents the SAW. . . . .	16
2.2	Toroidal coordinates [6]. . . . .	17
2.3	Alfvén Continuum for a toroidal and cylindrical configuration [7]. . . . .	18
2.4	Wave-Continuum interaction and mode form [7]. . . . .	19
2.5	Alfvén Continuum for stellarator equilibrium[8]. In black $\mathbf{n} = 1$ , red $\mathbf{n} = 2$ , green $\mathbf{n} = 3$ and blue $\mathbf{n} = 4$ . . . . .	20
3.1	Scheme representing the process from preparation to results analysis for <i>FAR3d</i> simulations. . . . .	23
3.2	Experimental profiles for TJ-II discharge #44257 in TJ-II device. . . . .	24
3.3	Scheme for the different scenarios studied with different NBI heating operations. . . . .	24
3.4	Scheme for the different scenarios studied with different magnetic topology. . . . .	25
3.5	Plasma density and temperature in TJ-II device. . . . .	28
3.6	Studied variations of NBI density with respect to the experimental profile. . . . .	29
3.7	Magnetic Topology Variation. . . . .	29
3.8	Resonant modes for #44257 experiment. . . . .	31
3.9	Resonant modes for the different topological variations of the magnetic field. . . . .	33
3.10	Eigenfunction for the perturbed electrostatic potential. . . . .	34
3.11	Simulations results plotted in the Alfvén continuum. . . . .	35
4.1	Heatmaps of growth rate (left) and frequency (right) of AE activity for the experimental profile. . . . .	40
4.2	Alfvén continuum for experimental $\iota$ calculated using <i>STELLGAP</i> code. . . . .	41
4.3	Alfvén activity for the experimental profiles. . . . .	42
4.4	Heatmaps of growth rate (left) and frequency (right) of AE activity for on-axis profile. . . . .	43
4.5	Heatmaps of growth rate (left) and frequency (right) of AE activity for Off-axis profile. . . . .	44
4.6	Alfvén activity for On-axis and Off-axis profile. . . . .	45
4.7	Electrostatic eigenfunctions for On-axis and Off-axis profile. . . . .	46

4.8	Growth rate (left) and frequency (right) of AE activity for high gradient profile. . . . .	47
4.9	Growth rate (left) and frequency (right) of AE activity for low gradient profile. . . . .	48
4.10	Alfvén activity in Alfvén continuum for high and low gradient profile. . . . .	49
4.11	Electrostatic eigenfunctions for High and Low gradient profiles. . . . .	50
4.12	Magnetic topology study of growth rate (left) and frequency (right). In purple $\Delta\iota = -0.45$ , in orange $\Delta\iota = -0.25$ , in red $\Delta\iota = 0.15$ , in green $\Delta\iota = 0.35$ . . . . .	53
4.13	$\Delta\iota$ Alfvén Continuum for the study of magnetic topology variations. . . . .	54
4.14	$n = 5, 9, 13, 17$ Alfvén activity for rotational transform profiles. . . . .	54
4.15	$n = 6, 10, 14$ Alfvén activity for rotational transform profiles. . . . .	55
4.16	$n = 7, 11, 15$ Alfvén activity for rotational transform profiles. . . . .	55

# Chapter 1

## Introduction

The global energy demand is increasing daily and is expected to grow near 50% by the year 2050 [9, 10] with a major predominance in fossil fuels (oil, coal and natural gas). Classical energy sources are not just insufficient to cover future needs but they are also one of the main agents with a negative impact on the environment [11, 12]. Continuing with nonrenewable sources may lead to adverse economic and environmental impacts.

Research for inexhaustible, continuous and clean energy sources without impact on the environment motivates the scientific community in a worldwide effort to address this crisis. Among the promising proposals, nuclear fusion appears in the energy paradigm as an efficient, virtually limitless and green fount with favorable characteristics to help solve these problems [13].

Compared to fossil fuels, nuclear fusion does not emit greenhouse gases. In addition, the fuel is available in large quantities, enough to supply the whole planet for a theoretically unlimited time. Its counterpart, nuclear fission, which relies on splitting heavy atoms, is an efficient source of energy, free of contaminating gases and safe. On the other hand, the management of radioactive wastes and the catastrophic scale consequences of nuclear accidents are major disadvantages. [14].

### 1.1 Nuclear Fusion

The mass of an atomic nucleus ( $m_z$ ) is not the sum of the masses of its Z-protons ( $m_p$ ) and A-Z neutrons ( $m_n$ ), with A the atomic mass number. On top of that, stable nuclides have a mass defect

$$\Delta = [Zm_p(A - Z)m_n] - Am_z \quad (1.1)$$

Einstein's mass-energy equivalence indicates that the mass difference can be seen as the necessary energy to disassemble the nucleus into its constituent parts, this is called *Binding Energy* [1]. Figure 1.1, shows the binding energy per nucleon. Divide nuclides with high mass number (A) to lower A-nuclides with larger  $\Delta$  is the basis of the fission process, merging two nuclides with low A to form a nucleus with higher A and larger  $\Delta$  per nucleon motivates the goal of fusion reactors.

If the reaction generates a net  $\Delta$ , the mass defect is invested in increasing the kinetic energy of the particles sub-product of the reaction.

$$\Delta E = (\Delta m)c^2 \quad (1.2)$$

The reaction that provides the largest difference in the binding energy is the fusion of Hydrogen into Helium, the main candidate to be the fuel of future nuclear fusion reactors.

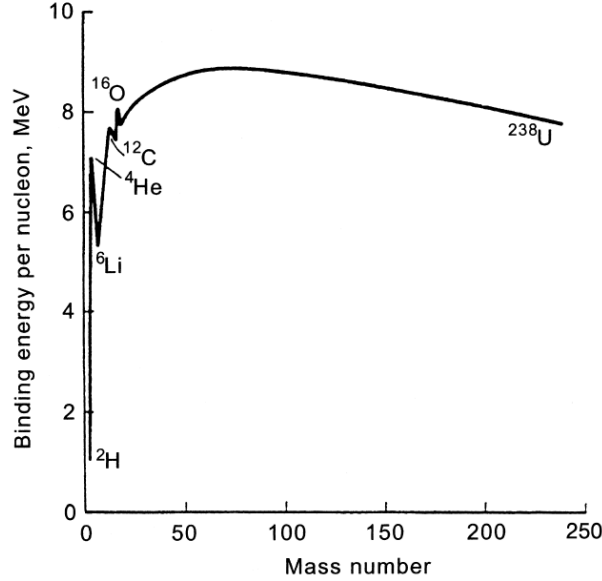


**Figure 1.1:** Binding Energy per nucleon vs Mass number (A) [1].

The velocity averaged cross-section ( $\langle \sigma v \rangle$ ) indicates the probability a reaction occurs. Figure 1.2 shows the velocity average cross-sections for the most promising reactions in nuclear fusion devices. Deuterium-tritium interaction shows the highest reaction probability at lower temperatures ( $\sim 70\text{keV}$ ).

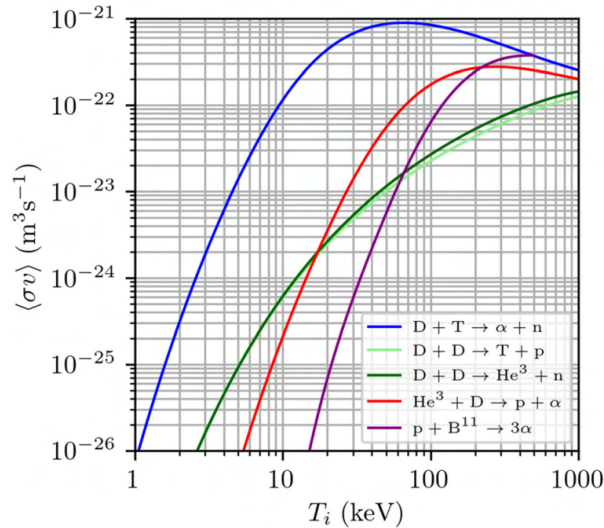
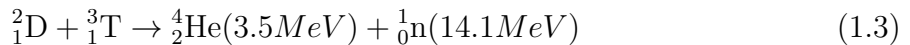


**Figure 1.2:** Velocity average cross-section for different reactions [2].

The reaction of D-T can be written as



Here, the masses of D and T are larger than the  $\text{He}$  and the neutron. A  $\Delta$  of  $17.5\text{MeV}$  is converted into kinetic energy, distributed according to momentum and energy conservation,  $\text{He}$ , also known as alpha particle ( $\alpha$ ), carries  $3.5\text{MeV}$  and the neutron has  $14.1\text{MeV}$ . For a fusion reactor to be feasible, reactions must be sustained for enough time, providing the required energy to burn the fuel. The reactions must generate enough energy to exceed the required for heating the fuel, hence high densities and good confinement

at temperatures of the order of  $10^8 - 10^9 K$  are critical. The fusion reactor operation requirement with respect to the fuel density ( $n$ ), temperature ( $T_e$ ) and confinement time ( $\tau_{E}$ ): [15] to generate net energy from fusion reactions. The Lawson criteria states [1],

$$nT_e\tau_E > 3 \cdot 10^{21} m^{-3} keVs \quad (1.4)$$

At these conditions, the matter is in a plasma state, an ionized gas composed of electrons and ions which is not possible to confine by a physical barrier due to its extremely high temperatures. However, since the gas is composed of charged particles, this condition can be exploited to achieve controlled and continuous reactions using large magnetic fields to confine the plasma.

## 1.2 Magnetic Confinement

The dynamic of a particle of species  $s$  with charge  $q_s$  and velocity  $\mathbf{v}$  under the influence of a magnetic field ( $\mathbf{B}$ ), is described by the Lorentz force [16]

$$m_s \frac{d\mathbf{v}}{dt} = q(\mathbf{E} + \mathbf{v}_s \times \mathbf{B}) \quad (1.5)$$

In the absence of an electric field ( $\mathbf{E}$ ), the particles will undergo a circular motion around the magnetic field lines (figure 1.3a) with a Larmour or cyclotron frequency given by

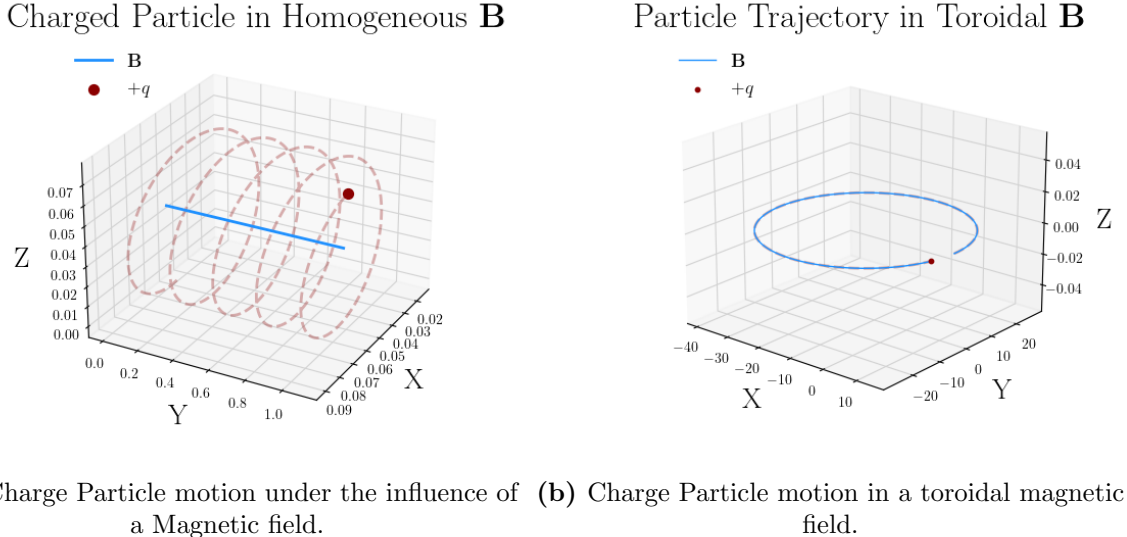


**Figure 1.3:** Charge particle dynamics in the presence of an external magnetic field.

$$\omega_c = \frac{|q_s|B}{m_s} \quad (1.6)$$

where  $m_s$  is the mass species. Since the magnetic field does no work, the perpendicular velocity ( $\mathbf{v}_{th,s}$ ) is constant and can be obtained as

$$\mathbf{v}_{th,s} = \sqrt{\frac{2T_s}{m_s}} \quad (1.7)$$

hence the radius of the particle's orbit also known as the Larmour radius results

$$r_L = \frac{\mathbf{v}_{th,s}}{\omega_c} \quad (1.8)$$

Since charged particles will follow magnetic field lines, it is possible to create a configuration that keeps the particles confined in a volume without hitting the walls of a vessel and be maintained for the necessary time at the required temperatures. A good geometry for this is using a torus configuration (figure 1.3b). However, toroidal curvature and nonuniformity of the field result in forces that generate a drift in the motion and lead to a radially outward movement. To compensate for this drift, a poloidal component of the magnetic field must be added that will make the particles follow a helical path around the torus. (Figure 1.4a) If a toroidal current (red arrows) is induced into the plasma, by Ampere's law a poloidal magnetic field is generated, leading to a helical motion (black) of the particles in combination with the toroidal magnetic field generated by the poloidal coils (green lines). This design of reactor is called Tokamak and historically is the most studied concept. The second way to proceed (Figure 1.4b) is generating the poloidal and toroidal components of the magnetic field by external coils. This concept is called stellarator and is the design that concerns this work.

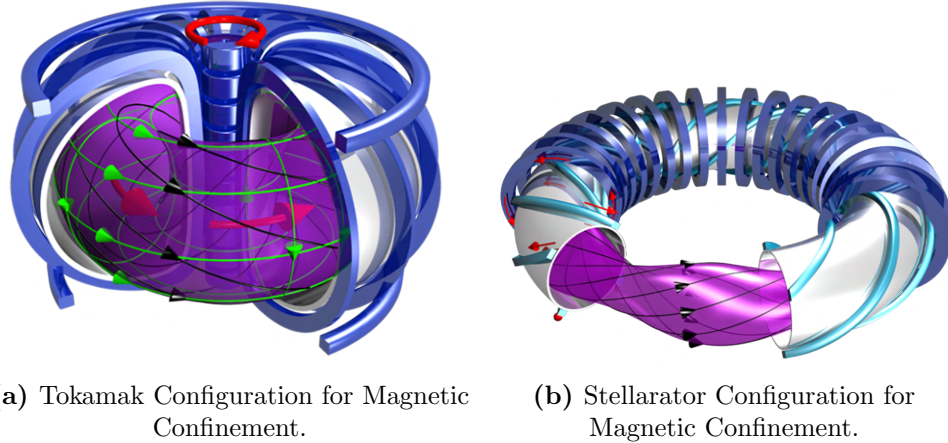


**Figure 1.4:** Plasma confinement concepts for nuclear reactors [3].

Theoretically, these configurations generate a series of toroidally nested magnetic closed flux surfaces. In stellarators (Figure 1.5b), these surfaces along the torus are indexed by the rotational transform

$$\frac{\iota}{2\pi} = \frac{d\phi}{d\Psi} \quad (1.9)$$

If the  $\iota$  profile shows a weak radial dependency it is said that the device has a low magnetic shear. In tokamaks (Figure 1.5a), the safety factor  $q = 1/\iota$  is used for the characterization of magnetic flux surfaces.

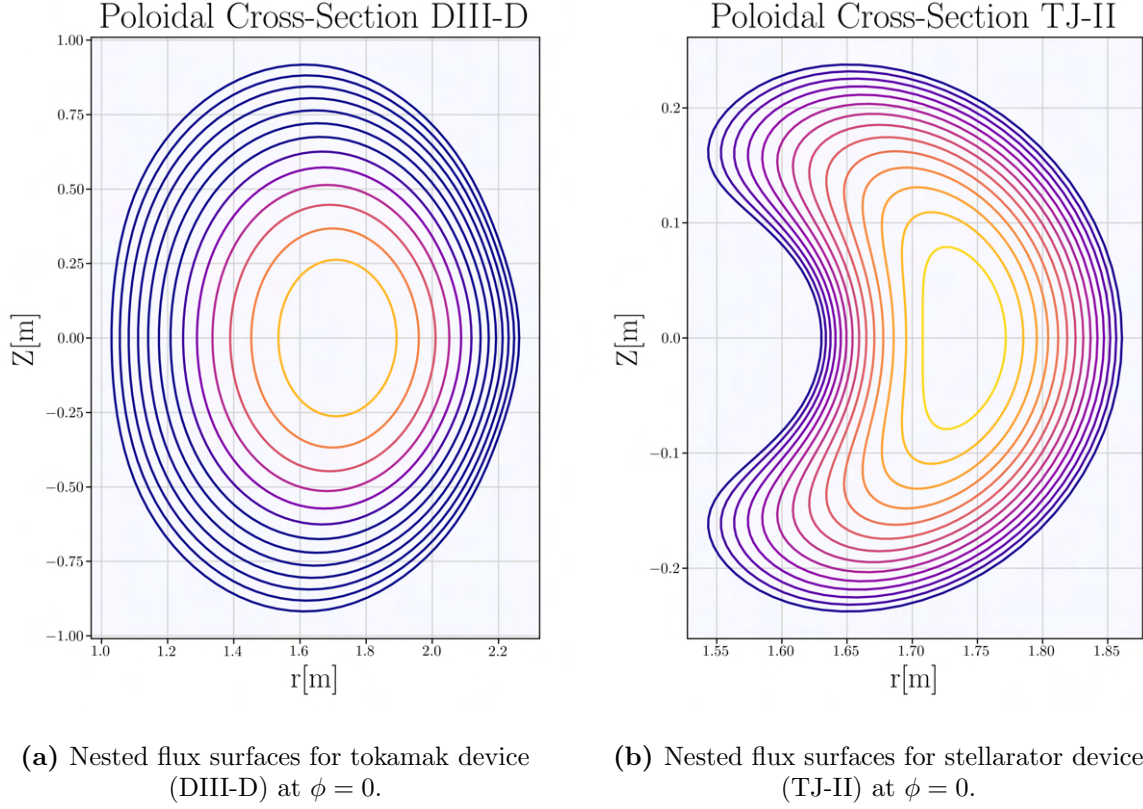


**Figure 1.5:** Nested magnetic closed flux surfaces generated with the [VMEC file](#).

## 1.3 Energetic Particles

Good confinement of alpha particles from reaction 1.3 is crucial to have a self-sustained burn. The energy from the  $\alpha$ 's is transferred to the thermal plasma, maintaining the temperature and the fusion reactions, this minimizes the external heating requirements and improves the nuclear reactor's economic viability. However, alpha's interaction with the plasma bulk can lead to the destabilization of Alfvén Eigenmodes (**AE**) that induce a partial loss of the alpha particle populations before thermalization [17].

Alfvén eigenmodes [4] are caused by the interaction of energetic particles (**EP**) with shear Alfvén waves, inherently present in the plasma. Not just alpha's, but EPs can be generated by the heating source of *Neutral Beam Injectors* (**NBI**) and radio frequency wave heating[18]. AEs are observed experimentally in different devices [19, 20] along with their effects [21]. Figure 1.6 shows a radial profile of electron temperature fluctuations and the safety factor profile ( $q$ ) in DIII-D tokamak. Reverse Shear Alfvén eigenmodes (RSAE) appear near the minimum value of  $q$  that extends radially and at higher frequencies, Toroidal Alfvén eigenmodes are observed.

Studying and understanding how **EPs** interact with the plasma is essential in the design and operation of future fusion reactors [22].

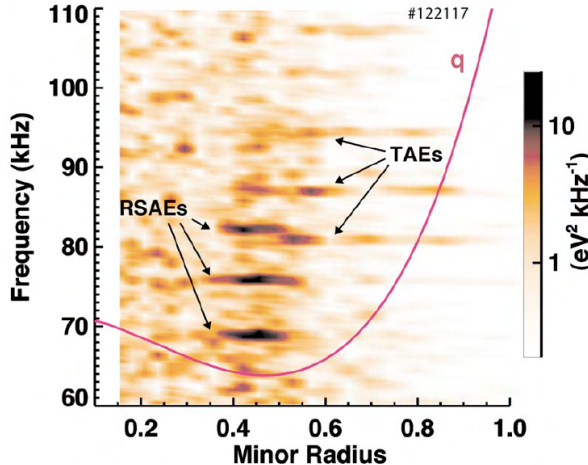


**Figure 1.6:** Two different AE identified in DIII-D discharge [4].

## 1.4 TJ-II Stellarator

At Laboratorio Nacional de Fusión in Madrid, Spain, is located the TJ-II stellarator device [23] of the heliac family. Figure 1.7a shows the shape of the TJ-II plasma (violet contour) and the device coils (blue color). In heliac devices, the center of the magnetic field coils is displaced following a helical field line[24]. Figure 1.7b shows the representation of a magnetic surface for this device. The TJ-II magnetic field has four-periods ( $N_{fp} = 4$ ) and it is designed to have a high rotational transform and low magnetic shear.

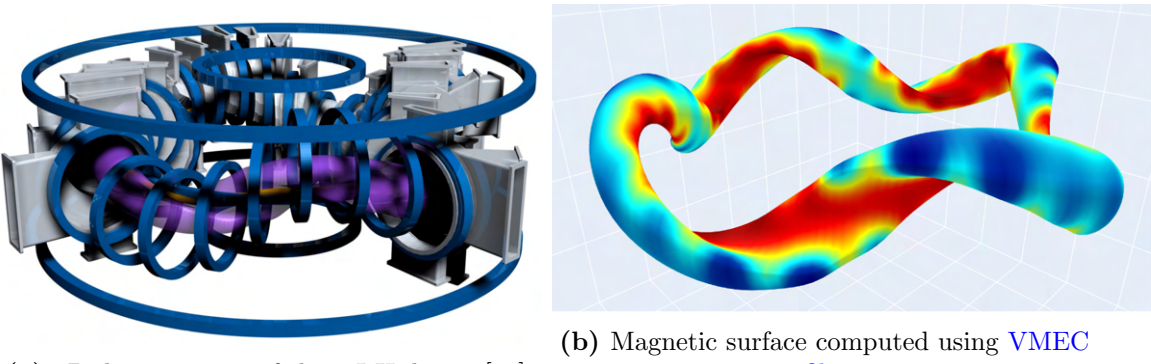


**Figure 1.7:** TJ-II Stellarator.

The major radius is  $R_0 = 1.5\text{m}$  and the average plasma radii is  $a = 0.22\text{m}$ . The central magnetic field strength is  $B_0 = 0.95\text{T}$ . Thermal electron and ion density are of the order of  $10^{19}\text{m}^{-3}$ . Thermal electron temperature reach almost 0.35 keV. TJ-II is designed to have a wide range of central rotational transform ( $0.9 \leq \iota(0) \leq 2.2$ ) [26].

Two hydrogen NBI (Figure 1.8), one co-injected with respect to the direction of the magnetic field (NBI1) and the other counter-injected (NBI2) [5] are used to increase the plasma temperature. Each injector provides a power of 700 kW with a maximum current and voltage of 60 A and 34 kV, respectively. Average NBI particle densities vary in the range  $0.5 - 1.0 \times 10^{19}\text{cm}^{-3}$  [27].

The presence of Alfvénic activity has been observed in TJ-II [27, 28]. As stated before, these instabilities reduce the heating efficiency of the NBI by increasing the EP transport leading to damage of the machine wall.

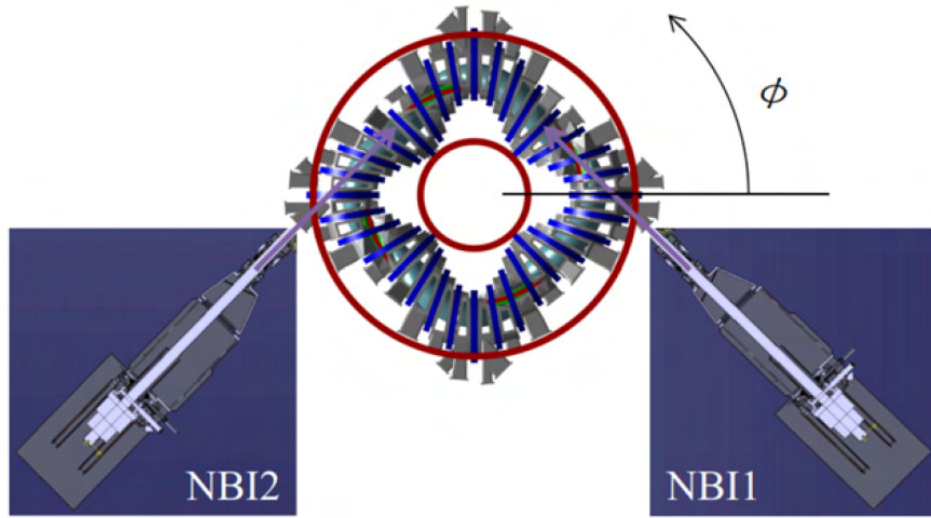


**Figure 1.8:** Eagle-view of TJII with schematics of the NBI heating systems [5].

## 1.5 Objectives and Structure

The study of Alfvén stability is required to identify optimum scenarios with respect to the AE activity because efficient plasma heating requires avoiding or minimizing the AE activities.

The main objective of this thesis is to study the linear stability of the AEs triggered by NBI energetic particles in the TJ-II stellarator. For this purpose, the *FAR3d* code is used.

The analysis for this work can be separated into two main parts.

- **NBI Operation Regime:** the AE stability is studied with respect to the NBI power injection (linked to the amount of EPs in the plasma), voltage (connected to the EP energy), and radial deposition region (comparing on-axis and off-axis configurations).
- **Magnetic Field Topology:** Alfvénic stability is studied for different rotational transform profiles.

The thesis structure is the following. **Section 2** shows basic the concepts about shear Alfvén waves (SAW) and the description of the SAW effects of the plasma in the frame of the magnetohydrodynamic theory (MHD). In addition, a brief introduction to the mechanisms of wave-particle interaction is provided. **Section 3** is dedicated to the description of the *FAR3d* code numerical model as well as the parameters used for simulations. This section also describes the Python libraries developed to analyze the simulation data. **Section 4** presents the main results of the simulations for the different analyses performed. Simulation results are discussed in **Section 5**. Conclusions are presented in **Section 6** along with proposed future research and improvements.



# Chapter 2

## Alfvén Eigenmodes Theory

The theory of Alfvén Eigenmodes is presented in order to have a fundamental understanding of Shear Alfvén waves (SAW) and their interaction with energetic particles (EPs).

### 2.1 Magnetohydrodynamic Theory

High-density plasmas (*Ideal Plasmas*) can be treated as a continuum in the velocity and position space (*Phase Space*). Aside from a common gas, the ionized characteristics of the medium make the plasma react to external electromagnetic fields.

The ideal Magnetohydrodynamics set of equations [29]

$$\frac{\partial \rho}{\partial t} + \nabla \cdot (\rho \mathbf{u}) = 0 \quad (2.1)$$

$$\rho \frac{d\mathbf{u}}{dt} = -\nabla P + \mathbf{J} \times \mathbf{B} \quad (2.2)$$

$$\frac{\partial P}{\partial t} + (\mathbf{u} \cdot \nabla) P + \gamma P \nabla \cdot \mathbf{u} = 0 \quad (2.3)$$

$$\frac{\partial \mathbf{B}}{\partial t} = -\nabla \times \mathbf{E} \quad (2.4)$$

$$\mu_0 \mathbf{J} = \nabla \times \mathbf{B} \quad (2.5)$$

$$\mathbf{E} = -\mathbf{u} \times \mathbf{B} \quad (2.6)$$

describe a plasma subject to Lorentzian forces. The variables represent the mass density ( $\rho$ ), pressure ( $P$ ), fluid velocity ( $\mathbf{u}$ ), magnetic field ( $\mathbf{B}$ ), electric field ( $\mathbf{E}$ ) and density current ( $\mathbf{J}$ ). The time evolution is determined for  $\rho$ ,  $P$ ,  $\mathbf{u}$  and  $\mathbf{B}$ .

The equation (2.1) represents the mass conservation, equation (2.2) is the momentum equation with  $d/dt$  the convective derivative, (2.3) is the energy equation, (2.4) is Faraday's law and equation (2.5) is Ampere's law. The last equation, (2.6) is the continuum Ohm's law. In this system, information about the velocity distribution function is averaged out, and the equations represent a continuous medium with zero net charge in position space[16].

Consider an homogeneous plasma in equilibrium with a magnetic field  $\mathbf{B} = B_0 \mathbf{e}_z$  in the z direction with current and velocity  $\mathbf{J} = \mathbf{u} = 0$  and plasma density and pressure  $P = P_0$  and  $\rho = \rho_0$ . If a small perturbation is applied to the plasma in the form

$$f = f_0 + \tilde{f}_1 \quad (2.7)$$

where  $\tilde{f}_1$  corresponds to an infinitesimal perturbation around the stability position  $f_0$ , then the quantities can be written as

$$\begin{aligned} P &= P_0 + \tilde{P}_1 \\ \rho &= \rho_0 + \tilde{\rho}_1 \\ \mathbf{u} &= \tilde{\mathbf{u}}_1 \\ \mathbf{B} &= \mathbf{B}_0 + \tilde{\mathbf{B}}_1 \\ \mathbf{J} &= \tilde{\mathbf{J}}_1 \end{aligned} \quad (2.8)$$

If equations are written in Fourier space  $\tilde{f}_1 = f_1 \cdot \exp[-i(\omega t - \mathbf{k} \cdot \mathbf{r})]$ , only keeping the first order terms, the following set of equations are obtained

$$\begin{cases} \frac{\partial \tilde{\rho}_1}{\partial t} + \rho_0 \nabla \tilde{\mathbf{u}}_1 = 0 \\ \frac{\partial \tilde{P}_1}{\partial t} + \gamma P_0 (\nabla \tilde{\mathbf{u}}_1) \\ \frac{\partial \tilde{\mathbf{B}}_1}{\partial t} = \nabla \times (\tilde{\mathbf{u}}_1 \times \mathbf{B}_0) \\ \mu_0 \tilde{\mathbf{J}}_1 = \nabla \times \tilde{\mathbf{B}}_1 \end{cases} \implies \begin{cases} \omega \rho_1 = \rho_0 (\mathbf{k} \cdot \mathbf{u}_1) \\ \omega P_1 = \gamma P_0 (\mathbf{k} \cdot \mathbf{u}_1) \\ \omega \mathbf{B}_1 = -\mathbf{k} \times (\mathbf{u}_1 \times \mathbf{b}_0) \\ \mu_0 \omega \mathbf{J}_1 = -i \mathbf{k} \times [\mathbf{k} \times (\mathbf{u}_1 \times \mathbf{b}_0)] \end{cases} \quad (2.9)$$

with  $\omega$  the frequency of the wave and  $\mathbf{k} = k_{\perp} \mathbf{e}_y + k_{\parallel} \mathbf{e}_z$  the propagating vector that lies in the  $(Y, Z)$  plane. From the momentum equation, separating by components

$$\begin{pmatrix} \omega^2 - k_{\parallel}^2 \mathbf{v}_A^2 & 0 & 0 \\ 0 & \omega^2 - k_{\perp}^2 \mathbf{v}_s^2 & -k_{\perp} k_{\parallel} \mathbf{v}_s^2 \\ 0 & -k_{\perp} k_{\parallel} \mathbf{v}_s^2 & \omega^2 - k_{\parallel}^2 \mathbf{v}_s^2 \end{pmatrix} \begin{pmatrix} u_x \\ u_y \\ u_z \end{pmatrix} = \begin{pmatrix} 0 \\ 0 \\ 0 \end{pmatrix}$$

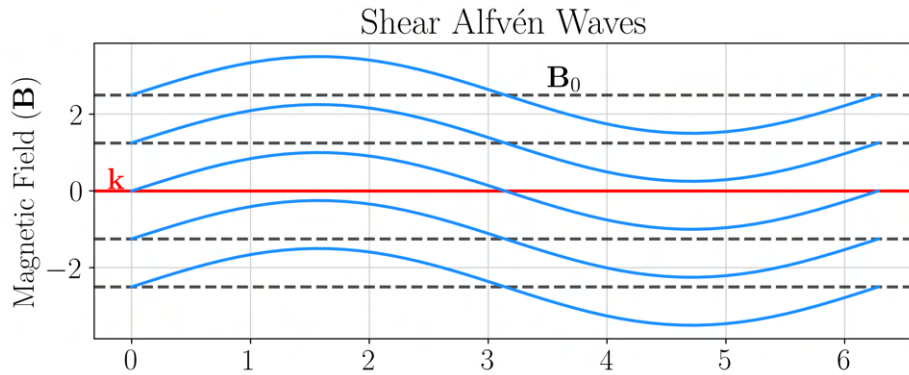


**Figure 2.1:** Line bending of the magnetic field that represents the SAW.

$\mathbf{v}_s = \gamma P_0 / \rho_0$  is the sound speed and  $\mathbf{v}_A$  the Alfvén speed. Computing the determinant of the system gives the dispersion relations

$$\begin{cases} \omega^2 = k_{\parallel}^2 \mathbf{v}_A^2 \\ \omega^2 = (1/2) k^2 (\mathbf{v}_A^2 + \mathbf{v}_s^2) [1 \mp (1 - \alpha^2)^{1/2}] \end{cases} \quad (2.10)$$

The first dispersion relation represents the shear Alfvén waves (SAW). These are purely transverse waves perpendicular to  $\mathbf{B}_0$  and  $\mathbf{k}$  (see Figure 2.1) that describe a line bending oscillation. SAW are incompressible, there are no fluctuations of density or pressure. The second dispersion relation has two solutions known as the fast magnetoacoustic waves (+ sign) and the slow magnetoacoustic waves (− sign). These waves are both compressional, affected by perturbations of density and pressure.

## 2.2 Shear Alfvén Waves

SAW are transverse low-frequency electromagnetic waves propagating along the magnetic field  $\vec{B}$  [7]. If the frequency of the wave ( $\omega$ ) results to be smaller than the ion cyclotron frequency ( $\Omega_i$ ), the dispersion relation can be written as

$$\omega = \mathbf{k}_{\parallel} \cdot \mathbf{v}_A \quad (2.11)$$

where the Alfvén speed is

$$\mathbf{v}_A = \frac{B}{\sqrt{\mu_0 \Sigma n_i m_i}} \quad (2.12)$$

From the dispersion relation 2.11, the group velocity  $\partial\omega/\partial k_{\parallel}$  equals the phase velocity, thus, SAW in uniform plasma are dispersionless.

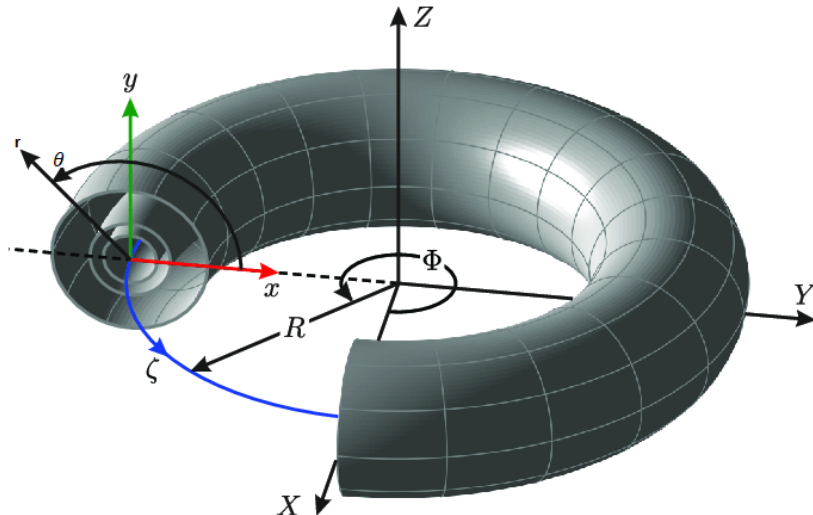


**Figure 2.2:** Toroidal coordinates [6].

SAW follow a helical path around the torus along the magnetic field lines. Thus, SAW can be labeled by the number of toroidal turns in the axial direction ( $\zeta$  in Figure 2.2) represented by  $\mathbf{n}$ , and poloidally by  $\mathbf{m}$  in the azimuthal direction ( $\theta$  in the figure). Then, if the magnetic field line rotates as  $\iota$  (or  $1/q$ ) times for a length period of  $2\pi R$  (torus circumference), then periodicity constraints impose

$$k_{\parallel} = \frac{n - m \cdot \iota(r)}{R} \quad (2.13)$$

As the rotational transform  $\iota(r)$  is a function of the minor radius  $r$ , this implies that the dispersion relation (2.11) is also a function of  $r$  for sheared  $\vec{B}$ . Hence, the dispersion relation can be written as

$$\omega = \left( \frac{n - m \cdot \nu(r)}{R} \right) \frac{B}{\sqrt{\mu_0 \Sigma n_i m_i}} \quad (2.14)$$

## 2.3 Alfvén Continuum

Toroidally confined plasma has periodic variations of the magnetic field and Alfvén velocity (orange lines in Figure 2.3) that cause openings in the frequency continuum (pink dashed lines in Figure 2.3), also called Alfvén Continuum [30]. This is analogous to the Bragg reflection: periodicity of the refraction index leading to band gaps.

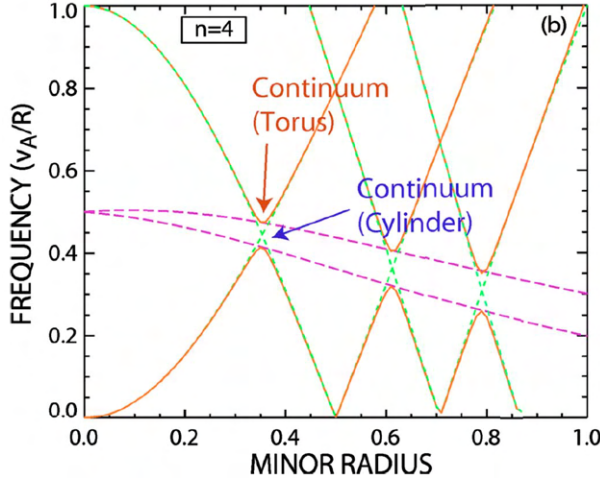


**Figure 2.3:** Alfvén Continuum for a toroidal and cylindrical configuration [7].

In fusion devices, magnetic mirror configuration results in periodic variations of the index of refraction

$$N = \frac{c}{v_\phi} = c \frac{\sqrt{\mu_0 \Sigma n_i m_i}}{B(r)} \quad (2.15)$$

where  $c$  is the speed of light and  $v_\phi = \mathbf{v}_A$  the phase velocity of the wave. This periodicity reflects off counter-propagating waves that interfere destructively to produce the gaps.

The Alfvén continuum has a stabilizing effect in SAW. Velocity variation along the radius for different waves makes perturbations disperse fast with a damping proportional to the gradient of the phase velocity ( $d\mathbf{v}_A/dr$ ). However, if the wave is not subject to continuum damping, interaction with energetic particles can trigger Alfvén waves to grow in the gaps.

Figure 2.4a represents a narrow wave because of the interaction with the continuum. For Figure 2.4b the wave is triggered in a gap below the continuum, the wave is wider and it is not affected by the continuum damping.

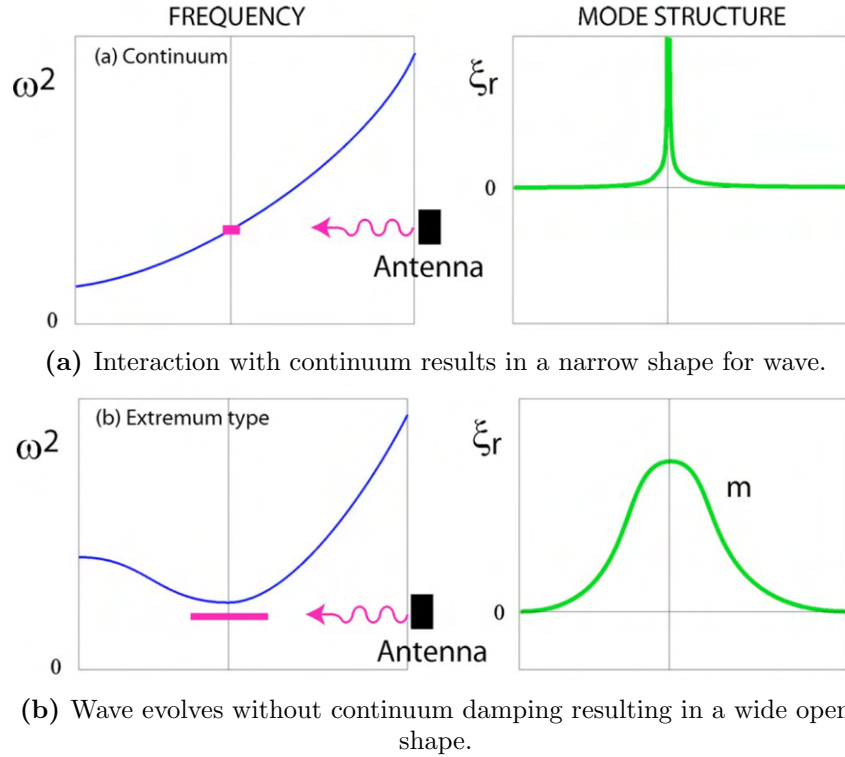


**Figure 2.4:** Wave-Continuum interaction and mode form [7].

## 2.4 Alfvén Waves Classification

Shear Alfvén eigenmodes (**AEs**) can be separated into two groups. In the first group are the AEs related to a minimum of the safety factor profile or an extrema of the continuum. Radial variation of the dispersion relation ( $\partial\omega/\partial r$ ) vanishes at the extrema of the rotational transform. Reverse Shear Alfvén Eigenmode (**RSAE**) presented in Figure 1.6 is an example of these modes. Global Alfvén Eigenmodes (**GAE**)<sup>[31]</sup> can be triggered nearby the continuum. Both AEs show as single dominant mode. Beta induced Alfvén Eigenmodes (**BAE**)<sup>[32]</sup> can be found below the continuum (see Figure 2.5).

The second group of AEs are caused by the interaction of counter-propagating waves. The coupling of waves with different **n** and **m** results in different AE families. Toroidal Alfvén eigenmodes (**TAE**) result from the coupling of **m** and **m+1** modes, with the same toroidal mode **n** (**n** modes with same color at low frequency in Figure 2.5).

Ellipticity (**EAE**)<sup>[33]</sup> and Noncircularity (**NAE**) Alfvén Eigenmodes are caused by the coupling of (**m, m+2**) and (**m, m+3** or higher) respectively, with the same **n**. As can be seen in Figure 2.5, EAEs and NAEs appear at higher frequencies. In addition, stellarator devices show Helicity Alfvén Eigenmodes (**HAE**) that results from the couplings of Alfvén waves  $n + iN_f$  with  $N_f$  the field period and  $i$  and integer. Figure 2.5 shows the coupling between different toroidal modes to form HAE.

Table 2.1 presents a summary of the different AEs that appear in fusion devices.

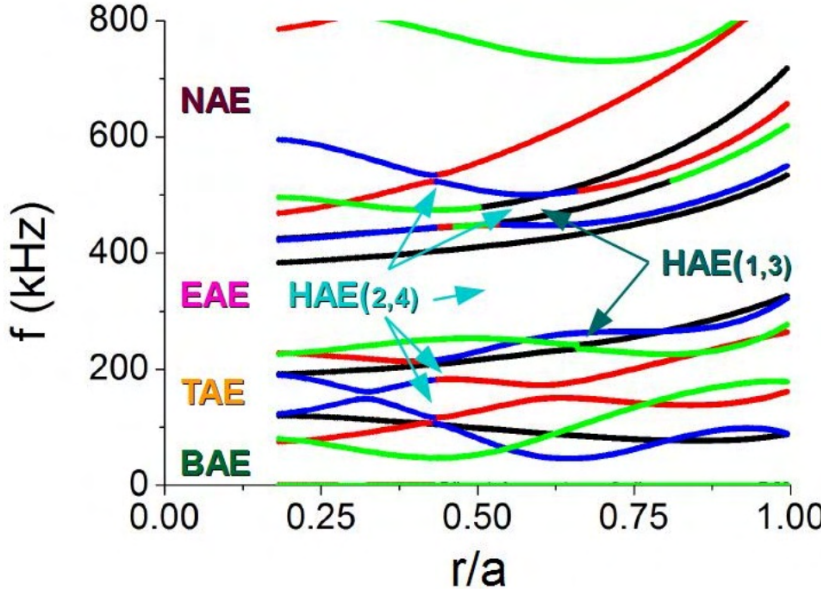


**Figure 2.5:** Alfvén Continuum for stellarator equilibrium[8]. In black  $\mathbf{n} = 1$ , red  $\mathbf{n} = 2$ , green  $\mathbf{n} = 3$  and blue  $\mathbf{n} = 4$ .

**Table 2.1:** Main Alfvén eigenmodes present in magnetic confinement devices.

Acronym	Name	Cause
RSAE	Reverse Shear	Minimum of $q$
BAE	Beta	Compressibility
GAE	Global	Generic Term
TAE	Toroidal	$m$ and $m+1$
EAE	Ellipticity	$m$ and $m+2$
NAE	Noncircularity	$m$ and $m+3$ (higher)
HAE	Helicity	$n + iN_{fp}$

## 2.5 Wave-Particle Energy Transfer

Interaction of EPs with SAW leads to the destabilization of AEs if the EP velocity is similar to the phase velocity of the SAW ( $\mathbf{v}_A$ ).

Energy transfer between particles and waves need

$$\mathbf{v} \cdot \mathbf{E} \neq 0 \quad (2.16)$$

Curved magnetic fields present drift motion of gradient and curvature

$$\mathbf{v}_d = \mathbf{v}_{\nabla B} + \mathbf{v}_C = \frac{mv_\perp^2}{2qB^3} \mathbf{B} \times \nabla \mathbf{B}(r) + \frac{mv_\parallel^2}{R_c^2} \frac{\mathbf{R}_C \times \mathbf{B}}{qB^2} \quad (2.17)$$

Curvature drift ( $\mathbf{v}_C$ ) goes to the square of the parallel velocity, for fast particles this term makes them deviate largely from the flux surfaces. Perpendicular electric field  $\mathbf{E}_\perp$

with respect to  $\mathbf{B}$  appears in fusion plasmas, and since drift velocity is also perpendicular to  $\mathbf{B}$  lines, energy transfer takes place. To have resonance, the orbit of the particle and the wave have to match. This condition can be written as

$$\omega + (m + l)\omega_\vartheta - n\omega_\phi = 0 \quad (2.18)$$

where  $\omega_\vartheta$  and  $\omega_\phi$  are the frequencies for poloidal and toroidal orbits respectively.  $l$  is an arbitrary integer,  $\mathbf{n}$  and  $\mathbf{m}$  are the toroidal and poloidal mode numbers. For example, for TAE centered at a frequency where the safety factor is

$$q = \frac{(m + 1/2)}{n} \quad (2.19)$$

with toroidal and poloidal frequencies

$$\omega_\phi = v_{||}/R \quad (2.20)$$

$$\omega_\vartheta = v_{||}/qR \quad (2.21)$$

Wave frequency can be written as

$$\omega = \frac{\mathbf{v}_A}{2qR} \quad (2.22)$$

in the resonance condition results

$$v_A + v_{||}(2l - 1) = 0 \quad (2.23)$$

two possible solutions are found for integer  $|l| = 1$ ,  $v_{||} = v_A$  and  $v_{||} = v_A/3$ . Only particles with a parallel velocity similar to Alfvén speed or a third of it can transfer their energy to the waves at a specific radial point. For co-going particles, one resonance will be with the  $\mathbf{m}$  harmonic and another with the  $\mathbf{m+1}$  that will interfere constructively to form the TAE [7].

In general, since AEs take their energy from the gradient of EP distribution function, their excitation usually requires an EP density gradient to be placed in the gaps where the AEs are allowed to grow. However, there are other factors that can determine energy exchange like the amplitude of poloidal harmonics or the alignment of the orbit with the AE.

The energy transfer is proportional to

$$\gamma \approx \omega \frac{\partial f}{\partial W} + n \frac{\partial f}{\partial P_\phi} \quad (2.24)$$

where  $f$  is the distribution function and  $P_\phi$  toroidal angular momentum. Fast particles with large  $\omega_\phi$  makes equation 2.18 to be satisfied by a large population.



# Chapter 3

## FAR3d and Analysis

The gyro-fluid FAR3d code is applied to study the linear AE stability in the TJ-II device. This chapter is dedicated to explaining the main features of FAR3d code and introducing the main parameters of the numerical model. In the last sub-section, the developed software for data analysis is presented.

### 3.1 Work Scheme

The linear study of Alfvénic activity in TJ-II stellarator was performed using the *FAR3d* code. *FAR3d* was developed by Oak Ridge National Laboratory and Universidad Carlos III de Madrid to study linear and nonlinear MHD stability in nuclear fusion devices. For this project, Alfvén activity was studied for different NBI operational regimes and variations in the magnetic topology. The first part is focus on studying Alfvén eigenmodes for different set-ups concerning the NBI heating systems. The second part addresses alternative magnetic configurations that will change the shape of gaps in the Alfvén continuum.

The aim of the study is identifying optimized operational regimes avoiding or minimizing the AE activity, improving the plasma heating efficiency and the device performance.

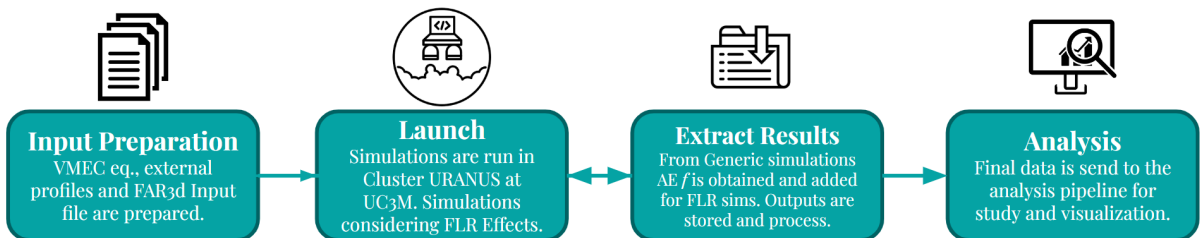
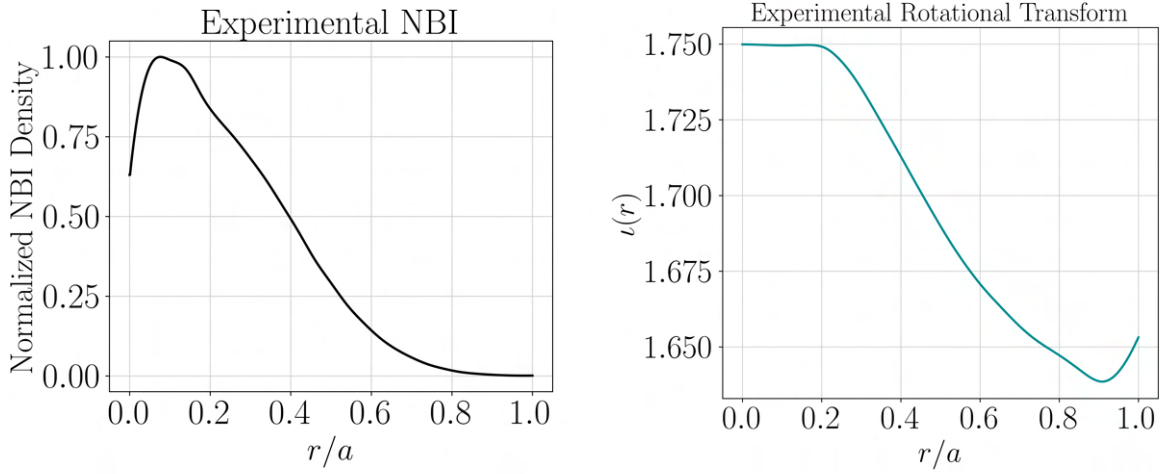


**Figure 3.1:** Scheme representing the process from preparation to results analysis for *FAR3d* simulations.

The work line for the simulation process is shown in Figure 3.1. To run *FAR3d*, 3 files must be provided. These are, a VMEC equilibrium in Boozer coordinates that contains the magnetic configuration of the device, the radial profiles for EP density ( $n_f$ ) and energy ( $T_f$ ), electron and ion density ( $n_e, n_i$ ) and temperature ( $T_e, T_i$ ). Finally, an *Input Model* file that contains the simulation specifications is prepared.

8 different scenarios with respect to experiment #44257 were performed. First, simulations are run using radial profiles of the EP density (Figure 3.2a) and energy, and iota

profile (Figure 3.2b) closer to the experiment.



(a) NBI Density profile for shot #44257.

(b)  $\iota$  profile for shot #44257.

**Figure 3.2:** Experimental profiles for TJ-II discharge #44257 in TJ-II device.

The simulation are performed for the helical families  $n = 5, 9, 13, 17$ ,  $n = 6, 10, 14$  and  $n = 7, 11, 15$ . The stability of each helical family is analyzed for different EP populations with respect to the EP energy  $T_f = [10, 15, 20, 25, 30, 35, 40, 45, 50]$  keV and EP beta of  $\beta_f = [0.1, 0.15, 0.2, 0.25, 0.3, 0.35, 0.4]$ .

Next, different NBI operations were simulated with respect to the beam deposition region and beam dispersion.(Figure 3.3). First by making a displacement in the axis, one close to the magnetic axis and the other near the plasma periphery. Finally, variations in the gradient of the NBI density profile are made, by increasing and lowering the slope.

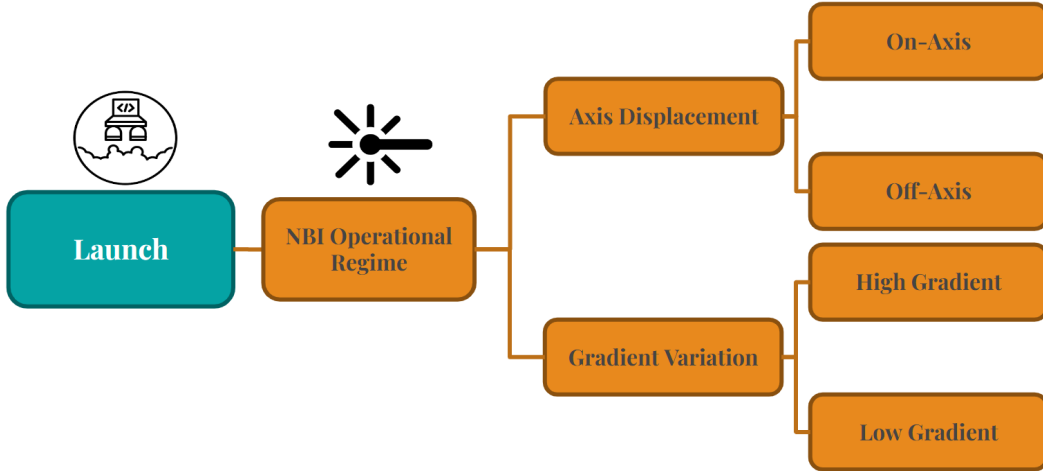


**Figure 3.3:** Scheme for the different scenarios studied with different NBI heating operations.

The final part concerns change in the magnetic field topology (Figure 3.4). Four variations of rotational transform were analyzed.

More than three thousand simulations were performed using the cluster of Universidad Carlos III de Madrid. To manage and analyze the data results, a series of *Python* libraries

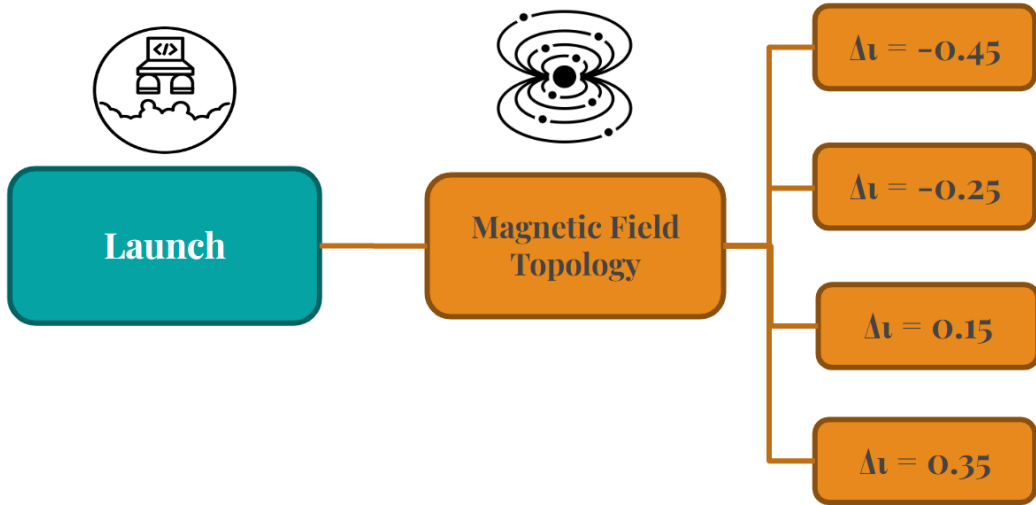


**Figure 3.4:** Scheme for the different scenarios studied with different magnetic topology.

were developed. This allows for an efficient and faster way to extract the relevant results. These libraries can be seen in my personal [repository](#).

## 3.2 Numerical Model

The FAR3d code solves a set of reduced MHD equations for a three-dimensional equilibrium adding Landau damping/growth (wave-particle resonance) and geodesic acoustic waves (parallel response of the thermal plasma). The effect of the EP perturbation is included as moments of the gyro-kinetic equation truncated with a closure relation [34], called Landau closure [35].

High aspect ratio ( $R/a$ ), medium  $\beta$  (in the order of the inverse aspect ratio  $\varepsilon = a/R$ ), small variation of the fields and small resistivity are assumed for the derivation of the reduced equations. The plasma velocity is defined as

$$\mathbf{u} = \sqrt{g} R_0 \nabla \zeta \times \nabla \Phi \quad (3.1)$$

and perturbation of the magnetic field results

$$\mathbf{B} = R_0 \nabla \zeta \times \nabla \psi \quad (3.2)$$

here  $\zeta$  represents the toroidal angle,  $\Phi$  is a stream function proportional to the electrostatic potential, and  $\psi$  is the perturbation of the poloidal flux.  $\sqrt{g}$  is the Jacobian of the coordinate transformation.

Equilibrium flux coordinates  $(\rho, \theta, \zeta)$  are used to describe the set of equations where  $\theta$  represents the poloidal angle, while  $\rho$  is the generalized radial coordinate proportional to the square root of the toroidal flux functions and normalized to one at the plasma edge. In dimensionless form, the set of MHD equations can be written as

$$\frac{\partial \tilde{\Psi}}{\partial t} = \sqrt{g} B \nabla_{||} \Phi + \frac{\eta}{S} \tilde{J}^{\zeta} - \frac{\beta_{0e}}{2\varepsilon^2 \omega_{cy} n} \sqrt{g} B \nabla_{||} p + \rho_i^2 \sqrt{\frac{\pi}{2}} \frac{v_A^2}{v_{th,e}} |\nabla_{||}| Q \quad (3.3)$$

$$\begin{aligned} \frac{\partial \tilde{U}}{\partial t} = & -v_{eq}^\zeta \frac{\partial \tilde{U}}{\partial \zeta} + \sqrt{g} B \nabla_\parallel J^\zeta - \frac{\beta_0}{2\varepsilon^2} \sqrt{g} (\nabla \sqrt{g} \wedge \nabla \tilde{p})^\zeta - \frac{\beta_f}{2\varepsilon^2} \sqrt{g} (\nabla \sqrt{g} \wedge \nabla \tilde{n}_f)^\zeta \\ & - \frac{\beta_\alpha}{2\varepsilon^2} \sqrt{g} (\nabla \sqrt{g} \wedge \nabla \tilde{n}_\alpha)^\zeta - \frac{\beta_{0i}}{2\varepsilon^2 \omega_{cy}} \sqrt{g} \left[ \nabla \wedge \left( \frac{\sqrt{g}}{B^2} (B \wedge \nabla p \cdot \nabla) v_\perp \right) \right]^\zeta \\ & + \omega_r \rho_i^2 \nabla_\perp^2 \tilde{U} - \frac{\beta_{oi}}{2\varepsilon^2 \omega_r} \tau_i p_{ieq} (S_{ei})_{imag} \Omega_d^2(\tilde{\Phi}) \end{aligned} \quad (3.4)$$

$$\frac{\partial \tilde{p}}{\partial t} = -v_{eq}^\zeta \frac{\partial \tilde{p}}{\partial \zeta} + \frac{dp_{eq}}{d\rho} \frac{1}{\rho} \frac{\partial \tilde{\Phi}}{\partial \theta} - \Gamma p_{eq} \nabla \cdot v - \frac{\Gamma \beta_{0i}}{2\varepsilon^2 \omega_{cy}} \frac{p_{i,eq}}{n} \nabla \tilde{p} \cdot \nabla \wedge \frac{B}{B^2} - \frac{\Gamma p_0 B_0}{\varepsilon^2 (J + uI)} \left( \frac{\partial}{\partial \theta} + \frac{\partial}{\partial \zeta} \right) v_{\parallel,th} \quad (3.5)$$

$$\frac{\partial \tilde{v}_{\parallel,th}}{\partial t} = -v_{eq}^\zeta \frac{\partial \tilde{v}_{\parallel,th}}{\partial \zeta} - \frac{\beta_0}{2n_{0,th}} \nabla_\parallel p \quad (3.6)$$

Here, equation 3.3 is the Ohms law,  $U = \sqrt{g} [\nabla \times (\rho_m \sqrt{g} \mathbf{v})]^\zeta$  represents the vorticity with  $\rho_m$  the mass density of the species.  $n_f$  (energetic particle density) is normalized to the density in the magnetic axis,  $\Phi$  is normalized to  $a^2 B_0 / \tau_{A0}$  and  $\Psi$  to  $a^2 B_0$ , with  $a$  the minor radius and  $\tau_{A0} = R_0 \sqrt{\mu_0 n_0} / B_0$  the Alfvén time. The time is normalized to the resistive time, the magnetic field to  $B_0$  (the averaged value at the magnetic axis), and the pressure to its equilibrium value at the magnetic axis ( $p_{eq}$ ). The Lundquist number  $S$  is the ratio of the resistive time to the Alfvén time.

$v_{\zeta,eq}$  is the equilibrium toroidal rotation,  $v_{\theta,eq}$  is the equilibrium poloidal rotation and  $v_{\parallel,th}$  is the parallel velocity of the thermal particles.

Now, for the Energetic Particles the moments results

$$\frac{\partial \tilde{n}_f}{\partial t} = -v_{eq}^\zeta \frac{\partial \tilde{n}_f}{\partial \zeta} - \frac{v_{th,f}^2}{\varepsilon^2 \omega_{cy}} \Omega_d(\tilde{n}_f) - n_{f0} \nabla_\parallel v_{\parallel f} - n_{f0} \Omega_d(\tilde{\Phi}) + n_{f0} \Omega_*(\tilde{\Phi}) + \varepsilon^2 \omega_r \omega_{cy} \frac{n_{f0}}{v_{th,f}^2} W - n_{f0} \Omega_*(W) \quad (3.7)$$

$$\frac{\partial \tilde{v}_{\parallel f}}{\partial t} = -v_{eq}^\zeta \frac{\partial \tilde{v}_{\parallel f}}{\partial \zeta} - \frac{v_{th,f}^2}{\varepsilon^2 \omega_{cy}} \Omega_d(\tilde{v}_{\parallel f}) - \sqrt{2} a_1 v_{th,f} |\nabla_\parallel \tilde{v}_{\parallel f}| - 2 a_0 \frac{v_{th,f}^2}{n_{f0}} \nabla_\parallel n_f + v_{th,f}^2 \Omega_*(\tilde{\Psi}) + v_{th,f}^2 \Gamma_f \Omega_*(\tilde{\Psi}) \quad (3.8)$$

$v_{th,f} = \sqrt{T_f/m_f}$  the energetic particle thermal velocity normalized to the Alfvén velocity in the magnetic axis and  $\omega_{cy}$  the energetic particle cyclotron frequency normalized to the Alfvén time.  $q_f$  is the charge,  $T_f$  the temperature and  $m_f$  the mass of the EPs.  $\mathbf{I}$  is the electric current and  $\mathbf{J}$  is the current density.

A set of auxiliary equations are used to take into account the effect of the EPs finite Larmour radius [36]

$$\begin{aligned} 0 &= Q - \nabla_\perp^2 \psi \\ 0 &= (1 + \rho_f^2 \nabla_\perp^2) W_{NBI} - \rho_f^2 \nabla_\perp^2 \Phi \\ 0 &= (1 + \rho_f^2 \nabla_\perp^2) X_{1,NBI} - \frac{\partial \psi}{\partial \zeta} \\ 0 &= (1 + \rho_f^2 \nabla_\perp^2) X_{2,NBI} - \frac{\partial \psi}{\partial \theta} \\ 0 &= (1 + \rho_f^2 \nabla_\perp^2) W_\alpha - \rho_f^2 \nabla_\perp^2 \Phi \\ 0 &= (1 + \rho_f^2 \nabla_\perp^2) X_{1,\alpha} - \frac{\partial \psi}{\partial \zeta} \\ 0 &= (1 + \rho_f^2 \nabla_\perp^2) X_{2,\alpha} - \frac{\partial \psi}{\partial \theta} \end{aligned} \quad (3.9)$$

The toroidal current density is defined as

$$J^\zeta = \frac{1}{\rho} \frac{\partial}{\partial \rho} \left( -\frac{g_{\rho\theta}}{\sqrt{g}} \frac{\partial \Psi}{\partial \theta} + \rho \frac{g_{\theta\theta}}{\sqrt{g}} \frac{\partial \Psi}{\partial \rho} \right) - \frac{1}{\rho} \frac{\partial}{\partial \theta} \left( -\frac{g_{\rho\rho}}{\sqrt{g}} \frac{\partial \Psi}{\partial \theta} + \rho \frac{g_{\rho\theta}}{\sqrt{g}} \frac{\partial \Psi}{\partial \rho} \right) \quad (3.10)$$

To model the average drift velocity of the passing particles, the operator  $\Omega_d$  is constructed as

$$\Omega_d = -\frac{v_{th,f}^2 v_A}{\omega_{cy} R_0} \left( \Omega_{dr} \frac{\partial}{\partial \rho} + \Omega_{d\theta} \frac{\partial}{\partial \theta} + \Omega_{d\zeta} \frac{\partial}{\partial \zeta} \right) \quad (3.11)$$

where:

$$\begin{aligned} \Omega_{dr} &= \frac{\sqrt{g}}{2\rho\varepsilon^2(J+\tau I)} \left( I \frac{\partial}{\partial \zeta} \frac{1}{\sqrt{g}} - \frac{\partial}{\partial \theta} \frac{1}{\sqrt{g}} \right) \\ \Omega_{d\theta} &= \frac{\sqrt{g}}{2\varepsilon^2(J+\tau I)^2} \left[ J \frac{\partial}{\partial \rho} (J+\tau I) \frac{1}{\sqrt{g}} - \beta_* \rho (J+\tau I) \frac{\partial}{\partial \zeta} \frac{1}{\sqrt{g}} \right] \\ \Omega_{d\zeta} &= \frac{\sqrt{g}}{2\rho\varepsilon^2(J+\tau I)^2} \left[ \beta_* \rho (J+\tau I) \frac{\partial}{\partial \theta} \frac{1}{\sqrt{g}} - I \frac{\partial}{\partial \rho} (J+\tau I) \frac{1}{\sqrt{g}} \right] \end{aligned} \quad (3.12)$$

And the diamagnetic drift frequency is conducted by

$$\Omega_* = \frac{T_f}{q_f B_0 a^2 \rho (J+\tau I)} \frac{1}{n_{0f}} \frac{dn_{0f}}{d\rho} \left( I \frac{\partial}{\partial \zeta} - J \frac{\partial}{\partial \theta} \right) \quad (3.13)$$

Equations (3.5) and (3.6) introduce the parallel momentum response of the thermal plasma. The equations (3.3) and (3.4) include the effect of the ion finite Larmour radius with  $\rho_i$  the thermal ions Larmor radius and  $v_{th}$  the ion thermal velocity. Equation (3.4) introduces the effect of the electron-ion Landau damping and collisions with  $\omega_r$  the frequency of the instability. In the equations (3.7) and (3.8) the effect of the energetic particle finite Larmour radius is added by the auxiliary equations (3.9). Equations (3.3) to (3.5) include the two fluid terms with  $\Lambda$  the electron pressure/total pressure ratio. The Boozer formulation is used for the flux coordinates where the Jacobian of the transformation is:

$$\sqrt{g} = \frac{J - uI}{B^2} \quad (3.14)$$

The code solves the system of equations by applying finite differences for the radial coordinate and Fourier expansion for the two angular variables [37].

### 3.3 Equilibrium Properties

The magnetic equilibrium is calculated using the VMEC code for the TJ-II discharge #44257 in which several MHD instabilities appear during the NBI phase ( $t \geq 1150$  ms) [27]. For the simulations, magnetic field intensity at the magnetic axis is  $B_0 = 0.95T$  was used, the major radius is  $R_0 = 1.5m$  and minor radius  $a = 0.22m$ .

The profiles of the thermal plasma used are presented in Figure 3.5. The electron and ion densities are shown on the left side of the figure, while the electron and ion

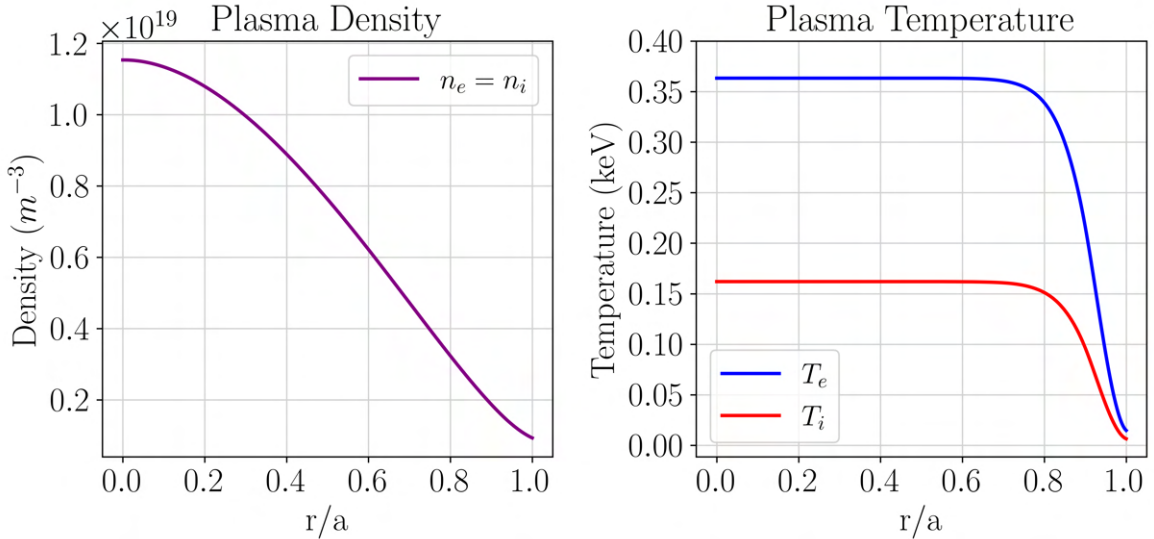
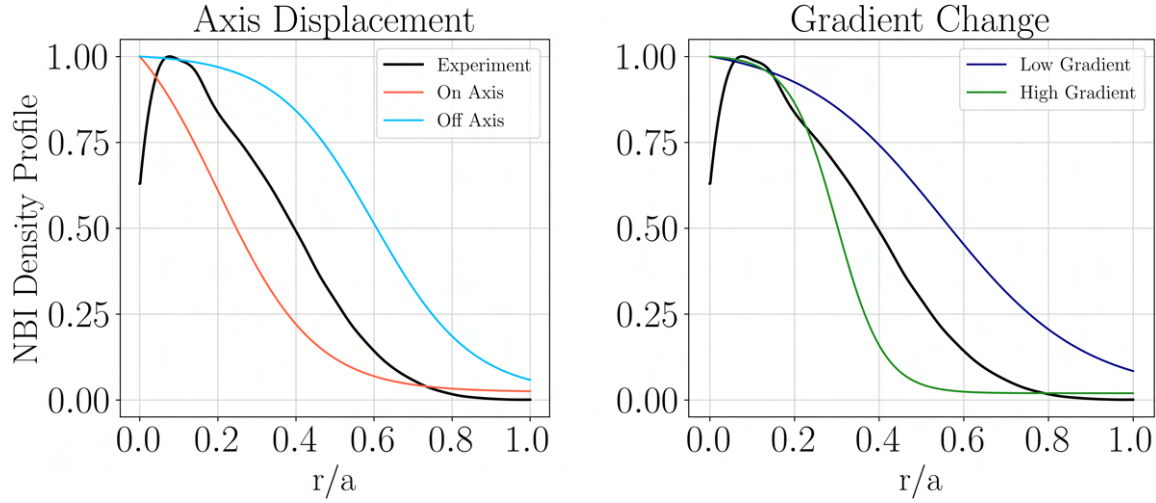


**Figure 3.5:** Plasma density and temperature in TJ-II device.

temperatures are shown on the right. These profiles are used for all simulation scenarios. For the study of NBI operational regime, the profiles of the rotational transform ( $\iota$ ) and NBI are shown in Figures 3.2a and 3.2b.

EP density profiles that represent different beam deposition regions are shown in Figure 3.6a, first near the magnetic axis (On-Axis in orange) and away from the magnetic axis (Off-Axis in sky blue). Then, the beam dispersion is analyzed modifying the EP density gradient shown in Figure 3.6b. Here, small beam dispersion (in green) and larger beam dispersion (in blue) gradient are used.

Finally, different rotational transform ( $\iota$ ) profiles are studied for the AE stability. These are shown in figure 3.7. In black can be seen the experimental  $\iota$ . Two  $\iota$  are taken below the experimental set, displaced by -0.45 (purple) and -0.25 (red). Then, two  $\iota$  profiles are taken above, displaced by 0.15 (orange) and 0.35 (green). The Alfvén continuum is computed using the code STELLGAP.



(a) Profiles used for study the NBI displacement effect in Alfvén activity. (b) Profiles used for study the gradient effect in Alfvén activity

**Figure 3.6:** Studied variations of NBI density with respect to the experimental profile.

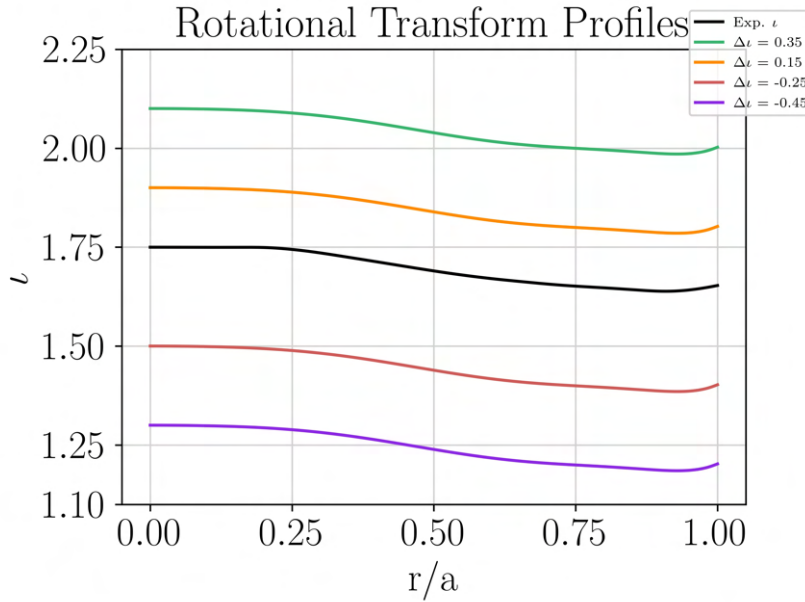


**Figure 3.7:** Magnetic Topology Variation.

## 3.4 Simulation Parameters

The Alfvén velocity ( $v_{A0}$ ) is  $4.85 \times 10^6$  m/s and the Alfvén time ( $\tau_{A0}$ ) is  $3.09 \times 10^{-7}$  s at the magnetic axis. The EP cyclotron frequency ( $\omega_{cyf}$ ) is 30.027 normalized to the Alfvén time at the magnetic axis. The magnetic Lundquist number is  $S = 5 \times 10^6$ . The radial grid is 1000. The resonance intensity is controlled by the ratio between the fast particles thermal velocity ( $v_{th,f}$ ) and Alfvén speed at the magnetic axis ( $v_{A0}$ ), resulting  $v_{th,f}/v_{A0}$ . Density profiles are normalized with respect to the density at the magnetic axis. Due to the periodicity of the TJ-II device ( $N_f = 4$ ), the coupling between the toroidal families is  $n = 5, 9, 13, 17$ ,  $n = 6, 10, 14$  and  $n = 7, 11, 15$ .

**Table 3.1:** Dynamical and equilibrium **n** and **m** modes used for NBI Operational Regime study.

<i>Dyn. Toroidal mode (n)</i>	<i>Poloidal mode (m)</i>
5	[2,4]
6	[3,5]
7	[3,6]
9	[4,7]
10	[5,8]
11	[5,9]
13	[6,10]
14	[7,11]
15	[7,11]
17	[9,13]
<i>Equil. Toroidal mode (n)</i>	<i>Poloidal mode (m)</i>
0	[0,5]
4	[0,5]
8	[2,7]
12	[5,10]

The toroidal and poloidal couplings used for the NBI operational regime study are presented in table 3.1. The column on the right first presents the dynamical **n** modes going from  $n = 5$  to  $n = 17$ ,

The dynamical toroidal modes used for this work go from  $n = 5$  to  $n = 17$ ,  $n = 0, 4, 8, 12$  are taken as equilibrium modes[38]. The toroidal modes  $n = 1, 2, 3$  are not included in the analysis because no resonant modes exist in the configurations analyzed, thus these modes energy is small.

For this study, the effect of the Finite Larmour Radius (**FLR**) is added. The Larmour radius for the energetic particles is obtained as

$$R_{L,f} = \frac{m_i v_{th,f}}{|q|B} \quad (3.15)$$

where the thermal speed is computed as

$$v_{th,f} = \sqrt{\frac{kT_f}{m_i}} \quad (3.16)$$

The Larmour radius is normalized to the minor radius  $a$ .

### 3.4.1 NBI Operational Regime Parameters

The toroidal and poloidal modes used for the NBI operational regime study are presented in table 3.1. The column on the right first shows the dynamical **n** modes and the equi-

librium modes  $n = 0, 4, 8, 12$ . In the right column,  $\mathbf{m}$  modes are shown.

Given the radial dependence of the  $\iota$  profile is possible to obtain the resonant modes for the system. This is shown in Figure 3.8. Here, resonant modes are  $n/m = 5/3$  and  $17/10$  for the families  $n = 5, 9, 13, 17$ . For  $n = 6, 10, 14$  family only  $n/m = 10/6$  and  $15/9$  for the  $n = 7, 11, 15$  helical couplings. Same members of the toroidal families are represented by the same color.  $n = 5, 9, 13, 17$  are in blue,  $n = 6, 10, 14$  have red color and  $n = 7, 11, 15$  appears in green.

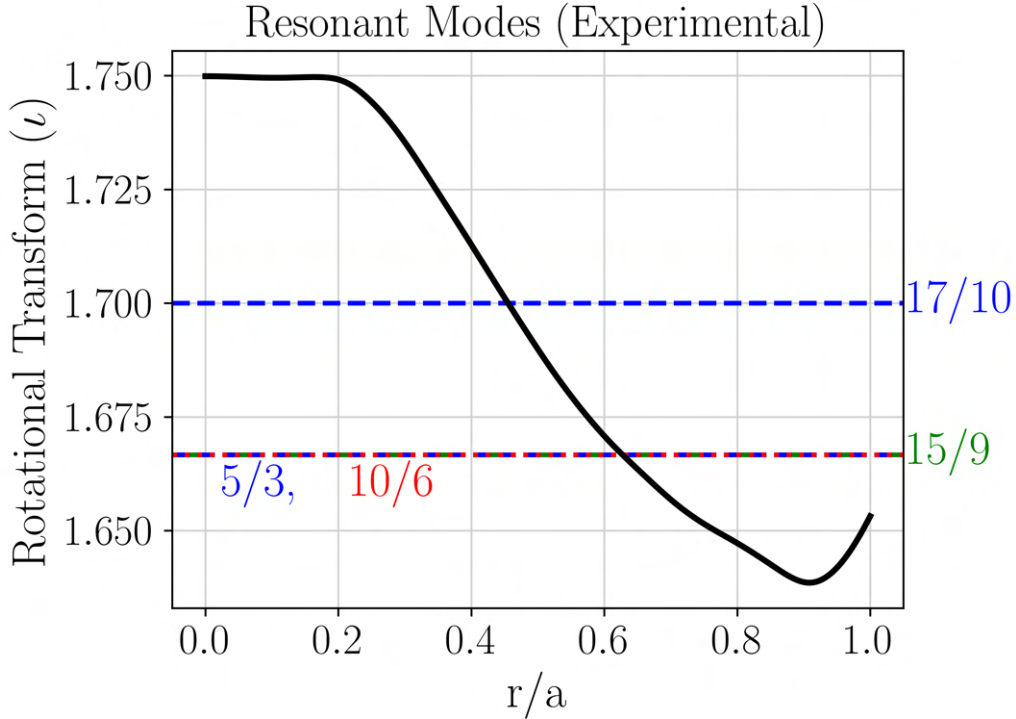


**Figure 3.8:** Resonant modes for #44257 experiment.

The values of  $\mathbf{R}_{L,f}$  used for this part are shown in table 3.2. The velocity ratio  $v_{th,f}/v_{A0}$  ranges from 0.215 to 0.481.

### 3.4.2 Magnetic Topology Parameters

The  $\mathbf{n}$  and  $\mathbf{m}$  modes used for this analysis are presented in table 3.3. Figure 3.9 presents the resonant modes for each of the 4 studied  $\iota$  profiles. Profiles with negative  $\Delta\iota$  show a larger number of resonant modes compared with positive  $\Delta\iota$ . Resonant modes for  $\Delta\iota = -0.45$  are shown in Figure 3.9a and for  $\Delta\iota = -0.25$  in Figure 3.9b. Toroidal mode  $n = 3$  is added to this profile due to resonance of mode  $n/m = 3/2$ .

Positive  $\Delta\iota$ ,  $\Delta\iota = 0.15$  (Figure 3.9c) shows resonance for families  $n = 9, 13, 17$  and  $n = 11, 15$ , while  $\Delta\iota = 0.35$  (Figure 3.9d) only have presence of resonant modes for  $n = 6, 10, 14$ .

**Table 3.2:** Finite Larmour radius for NBI heating and Magntic Topology study.

$T_f$ [keV]	$R_{L,f}$ [m]
10	0.0489
15	0.0598
20	0.0691
25	0.0772
30	0.0846
35	0.0914
40	0.0977
45	0.1036
50	0.1092

**Table 3.3:** Dynamical and equilibrium toroidal and poloidal modes for different rotational transform profiles.

<b>Dyn. <math>n</math></b>	<b><math>m</math> (<math>\Delta\iota = -0.45</math>)</b>	<b><math>m</math> (<math>\Delta\iota = -0.25</math>)</b>	<b><math>m</math> (<math>\Delta\iota = 0.15</math>)</b>	<b><math>m</math> (<math>\Delta\iota = 0.35</math>)</b>
3	—	[1,3]	—	—
5	[3,5]	[2,5]	[2,4]	[2,4]
6	[4,6]	[2,5]	[3,5]	[2,6]
7	[4,6]	[3,6]	[3,5]	[2,5]
9	[5,8]	[4,8]	[4,6]	[3,7]
10	[6,9]	[3,8]	[4,7]	[2,8]
11	[7,10]	[4,9]	[5,8]	[4,8]
13	[7,11]	[6,11]	[6,9]	[5,9]
14	[9,13]	[7,12]	[6,9]	[5,12]
15	[10,14]	[6,11]	[6,10]	[6,10]
17	[10,14]	[9,14]	[7,11]	[7,12]
<b>Equil. <math>n</math></b>	<b><math>m</math> (<math>\Delta\iota = -0.45</math>)</b>	<b><math>m</math> (<math>\Delta\iota = -0.25</math>)</b>	<b><math>m</math> (<math>\Delta\iota = 0.15</math>)</b>	<b><math>m</math> (<math>\Delta\iota = 0.35</math>)</b>
0	[0,5]	[0,5]	[0,5]	[0,5]
4	[0,5]	[0,5]	[0,5]	[0,5]
8	[2,7]	[2,7]	[2,7]	[2,7]
12	[5,10]	[5,10]	[5,10]	[5,10]

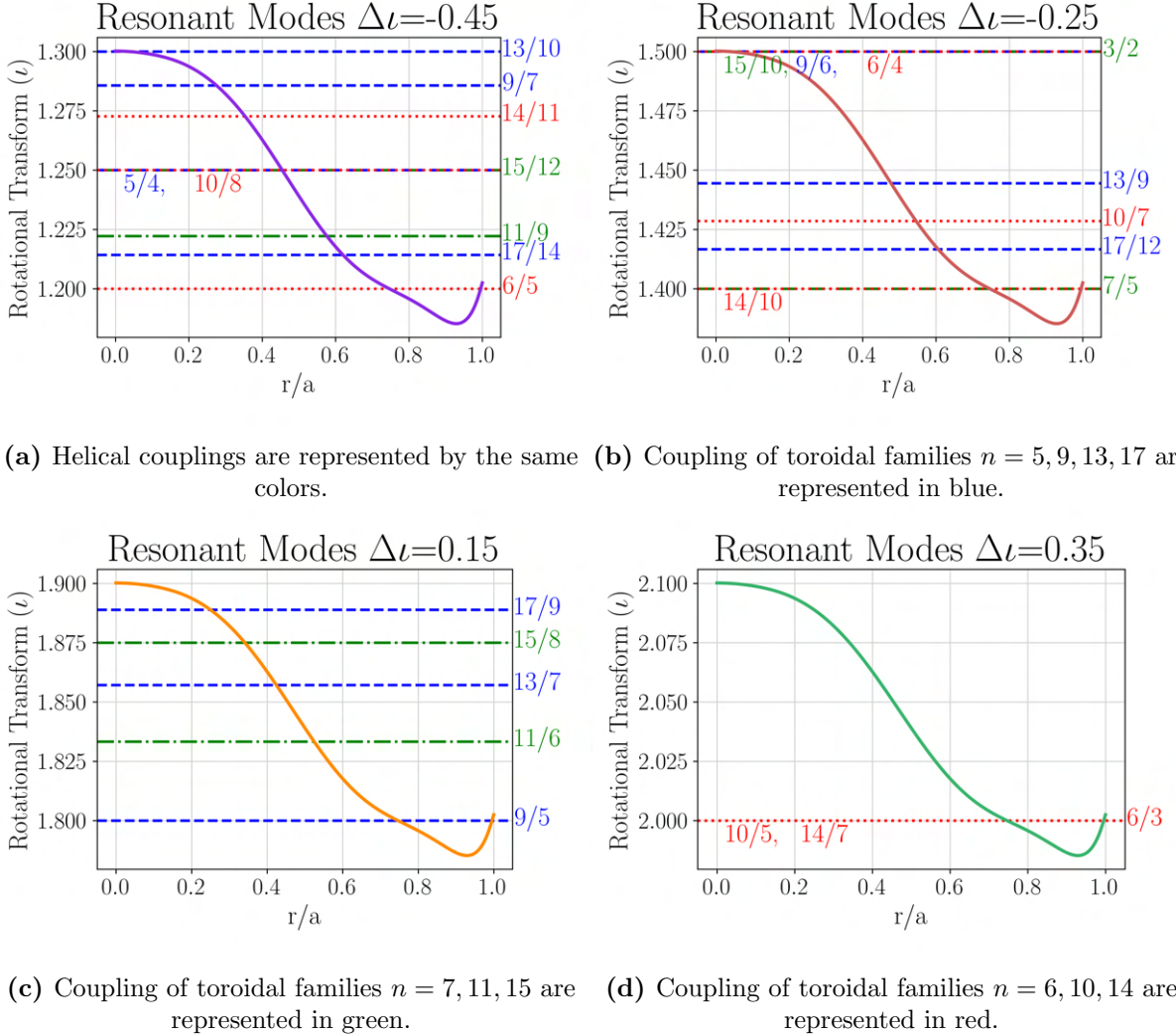


**Figure 3.9:** Resonant modes for the different topological variations of the magnetic field.

## 3.5 Data Acquisition and Analysis Libraries

*FAR3d* returns an important amount of data from their outputs. To efficiently [extract](#) and [analyze](#) what is relevant for this work, *Python* libraries were developed.

One *FAR3d* simulation, returns radial profiles for the pressure, magnetic flux, EP density, plasma and EP thermal velocities, and electrostatic potential ( $\delta\Phi$ ) as well as frequency and growth rate for the modes.

Figure 3.10 shows an example of the electrostatic potential eigenfunction for an EPs energy of 10 keV and  $\beta_f$  of 0.2. The AE frequency is 96 kHz. The plot shows the modes with the higher amplitude or dominant modes. For this case  $n/m = 15/10$  in sky blue color and  $11/7$  in magenta are coupled, thus the mode is an HAE. *FAR3d* eigenfunctions are represented in terms of sine and cosine component as

$$f(\rho, \theta, \zeta, t) = \sum_{n,m} f_{mn}^s(\rho, t) \sin(m\theta + n\zeta) + \sum_{n,m} f_{mn}^c(\rho, t) \cos(m\theta + n\zeta) \quad (3.17)$$

which represents positive and negative values of  $\mathbf{n}$  mode numbers [39]. In Figure 3.10, this is represented by dashed lines for the sine solution and with solid lines for the cosine solution.

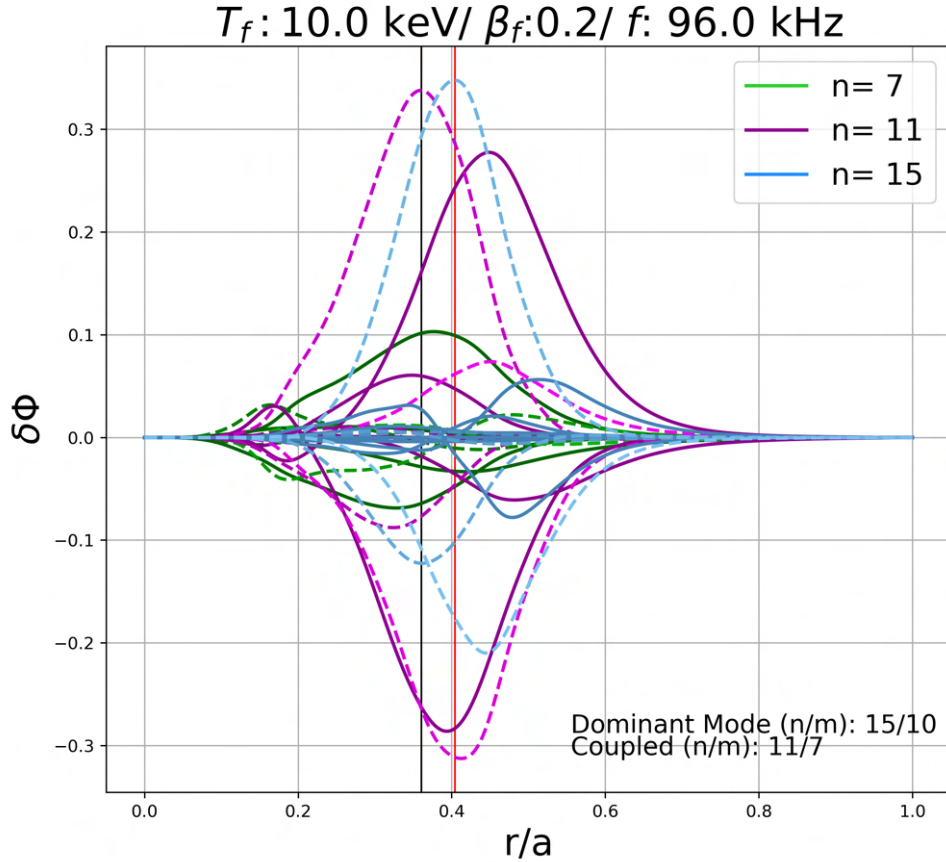


**Figure 3.10:** Eigenfunction for the perturbed electrostatic potential.

The *Python* script returns a dataset containing the  $T_f$ ,  $\beta_f$ , the dominant mode, the radial position, and the width of the eigenfunction, the second dominant mode and its radial position, the growth rate of the AEs, the angular frequency and the frequency in kHz. Also, it plots the eigenfunction as Figure 3.10.

Once the data have been extracted, it is sent to the analysis pipe line. Here the results stored in the dataset are processed and then plotted in an Alfvén continuum (Figure 3.11). This allows for identification of AEs and tendencies. The analysis code also obtains the values of  $T_f$  and  $\beta_f$  where the growth rate is maximum for a scenario.

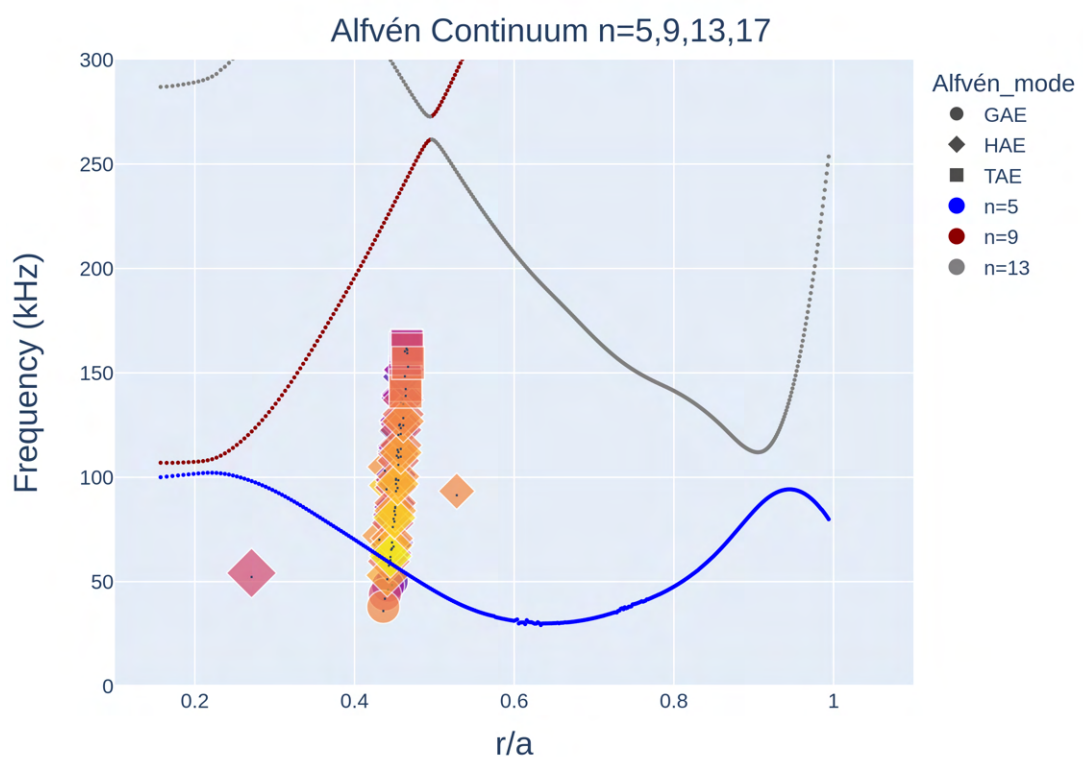


**Figure 3.11:** Simulations results plotted in the Alfvén continuum.



# Chapter 4

## Results

### 4.1 NBI Density Profile Variation

Figure 4.1 shows the **AE** growth rate ( $\gamma\tau_A$ ) and frequency ( $f(\text{kHz})$ ) as function of **EP** beta and energy. The **AE** growth rate is similar for the different helical families. Increase in  $\beta_f$  (larger **EP** density in the plasma) results in a higher growth rate. Increasing the energy leads to an increase of the **AE** growth rate if the **EP** resonance is enhanced. **FLR** effects reduces **AE** instability, reducing the available free energy in the system to trigger instabilities. Helical families  $n = 5, 9, 13, 17$ ,  $n = 6, 10, 14$  and  $n = 7, 11, 15$  reach the highest growth rate if  $T_f = 20 \text{ keV}$  and  $\beta_f = 0.4$ . For the helical family  $n = 5, 9, 13, 17$  (Figure 4.1a), mode frequency ranges between [37,163] kHz. **AEs** are stable (dark region) if  $T_f \geq 40 \text{ keV}$  for  $\beta_f (0.1, 0.15)$ . Helical family  $n = 6, 10, 14$  (Figure 4.1b) presents a range of frequencies from [41,254] kHz and **AEs** are stable if  $T_f \geq 30 \text{ keV}$  and  $\beta_f \leq 0.2$ .  $n = 7, 11, 15$  (Figure 4.1c) frequencies range between [48,231] kHz and the **AE** are stable if  $T_f \geq 35 \text{ keV}$  and  $\beta_f = 0.1$  and  $0.4$ .

4.2 shows the continuum gaps for each helical family. The Alfvén gaps show a large variability with respect to the radial location and toroidal mode number. The **BAE** gaps range between 5 to 300 kHz and the TAE gaps are observed between 300 to 400 kHz.  $n = 5, 9, 13, 17$  presents two **HAE** gaps (black ovals 1 and 2), at 230 kHz for toroidal modes  $n = 9, 13$  around  $r/a = 0.5$  and at 148 kHz for  $n = 15, 13$  around  $r/a = 0.65$ . The helical family  $n = 6, 10, 14$  shows two **HAE** gaps (cyan ovals 3 and 4) at 313 kHz and  $r/a = 0.66$  for  $n = 6, 14$  and near 113 kHz for  $n = 10, 14$  at  $r/a = 0.4$ . Family  $n = 7, 11, 15$  presents **HAE** at 158 kHz and  $r/a = 0.64$  for  $n = 3, 7$  and at 233 kHz and  $r/a = 0.33$  for  $n = 11, 15$ .

Once the gaps are identified, the **AEs** can be classified. Figure 4.3 shows the **AEs** for the different helical families. In the figure, red color indicates **BAEs** and cyan color the **GAEs**. The dominant mode is showed.

Figure 4.3a indicates the **AEs** triggered by the helical family  $n=5,9,13,17$  are located around  $r/a = 0.45$ .  $n/m = 5/3$  **BAE** is unstable if  $T_f = 10 \text{ keV}$  and  $\beta_f = 0.4$ .  $9/5$  **GAE** is triggered by  $T_f = 10 \text{ keV}$  and  $\beta_f = 0.3$  as well as  $T_f = 15 \text{ keV}$  and  $\beta_f = 0.35, 0.4$ . AE 13/8 is destabilized by an  $T_f = 10 \text{ keV}$  and  $\beta_f = 0.35$ . Wide 5/3 **BAEs** are triggered if  $T_{15}$  to 50 keV).  $n = 6, 10, 14$  are indicated in figure 4.3b, unstable around  $r/a = 0.51$ . **BAE** 6/4 is unstable if  $\beta_f$  goes from 0.2 to 0.4 and for all **EP** energies tested. 14/8 **GAE** is identified if  $T_f = 10 \text{ keV}$  and **EP** beta 0.4. The **AEs** triggered by the helical family  $n = 7, 11, 15$  are located around  $r/a = 0.45$ . 7/4 **GAEs** is unstable if  $T_f \geq 15 \text{ keV}$  and  $\beta_f = [0.1 - 0.4]$ . If  $T_f = 10 \text{ keV}$  and  $\beta_f = 0.4$ , 15/9 **GAE** is triggered.  $n/m = 11/6$  is obtained for  $T_f = 10, 15 \text{ keV}$  ad **EP** beta of 0.35 and 0.4 respectively.

### 4.1.1 NBI Axis Displacement

AE  $\gamma$  and  $f$  are shown in figure 4.4 for on-axis and 4.5 for off-axis. The lowest **AE** growth rate are calculated for the on-axis configurations.  $n = 5, 9, 13, 17$  **AEs** (figure 4.4a) are stable if  $T_f = 30$  to 50 kev and  $\beta_f \leq 0.3$ .  $n = 6, 10, 14$  (figure 4.4b) and  $n = 7, 11, 15$  (figure 4.4c) are stable if  $T_f = 10 - 50$  keV for  $\beta_f \leq 0.25$  and  $T_f = 30 - 50$  kev for  $\beta_f \leq 0.3$  respectively.  $n = 6, 10, 14$  shows frequencies from [47,289] kHz. Large frequencies are obtained at 50 keV and higher beta values from 0.3 to 0.4.  $n = 6, 10, 14$  shows frequencies range of [55,235] kHz with high frequencies at 50 keV and beta values of 0.35 to 0.4.

Off-axis profile results are shown in figure 4.5. Helical family  $n = 5, 9, 13, 17$  (Figure 4.5a) shows stable **AE** if  $\beta_f \leq 0.1$  and  $T_f = 45, 50$ .  $n = 6, 10, 14$  (Figure 4.5b) shows stable **AEs** if  $T_f = 45, 50$  and  $\beta_f \leq 0.15$ . For the helical family  $n = 7, 11, 15$  (Figure 4.5c) frequencies **AEs** are stable if  $T_f \geq 40$  keV.

Figure 4.6 shows frequency range and radial location of the unstable **AEs** with respect to the continuum gaps. On-axis profile results are represented as a vertical line at the left, off-axis results have a vertical line at the right. Dominant mode is presented above the line. The EP energy that triggers the **AE** is at the side. In green color are represented the **GAEs**, in red the **BAEs**. Helical family  $n = 5, 9, 13, 17$  is shown in figure 4.6a. For on-axis case, average radial position is  $r/a = 0.28$  and average radial width of 0.15. Off-axis average radius is  $r/a = 0.62$  and width 0.2. If  $T_f = 10$  keV 5/3 **BAE** is trigger for on-axis case. If  $T_f = 10$  in the off-axis profile, 13/8 **BAE** at  $\beta_f = 0.35$  and 5/3 **GAE** for different EP beta are trigger. If  $T_f \geq 15$  keV, 5/3 **GAEs** are trigger for both profiles. Helical family  $n = 6, 10, 14$  (Figure 4.6a) shows **AEs** average radial position at  $r/a = 0.26$  and 0.67 for on-axis and off-axis respectively. Average width of the **AEs** is 0.13 for on-axis profile and 0.19 for off-axis. On-axis 14/8 – 10/6 **HAE** (figure 4.11c) and 10/6 **GAE** are trigger if  $T_f = 10$  keV and  $\beta_f = 0.1$  and 0.15 respectively. 6/4 **BAE** are observed for the rest of the parameters. At middle plasma, 10/6 **GAE** (figure 4.11d) are triggered if  $\beta_f \leq 0.2$  and  $T_f \geq 10$  keV. 6/4 **BAE** become unstable  $\beta_f \geq 0.25$  and  $T_f \geq 10$  keV. On axis profile shows unstable 7/4 **BAEs** (figure 4.11e) for all  $T_f$  and  $\beta_f$  at radial average position of 0.31. Average width is 0.14. For off-axis case, mean position and extension is  $r/a = 0.6$  and 0.18. 7/4 **BAE** is trigger if  $T_f$  is in range of 10 to 20 keV. 15/9 **GAE** (figure 4.11f) is unstable for  $T_f = 10, 15$  keV and at  $\beta_f = 0.1$  and in the range of 0.3 to 0.4. 7/4 **GAE** are triggered for  $T_f \geq 40$ .

Deposition of particles at a radial position where gaps in the continuum are wide results in a larger drive by the EPs and **AE** growth rates.

### 4.1.2 NBI Gradient Variation

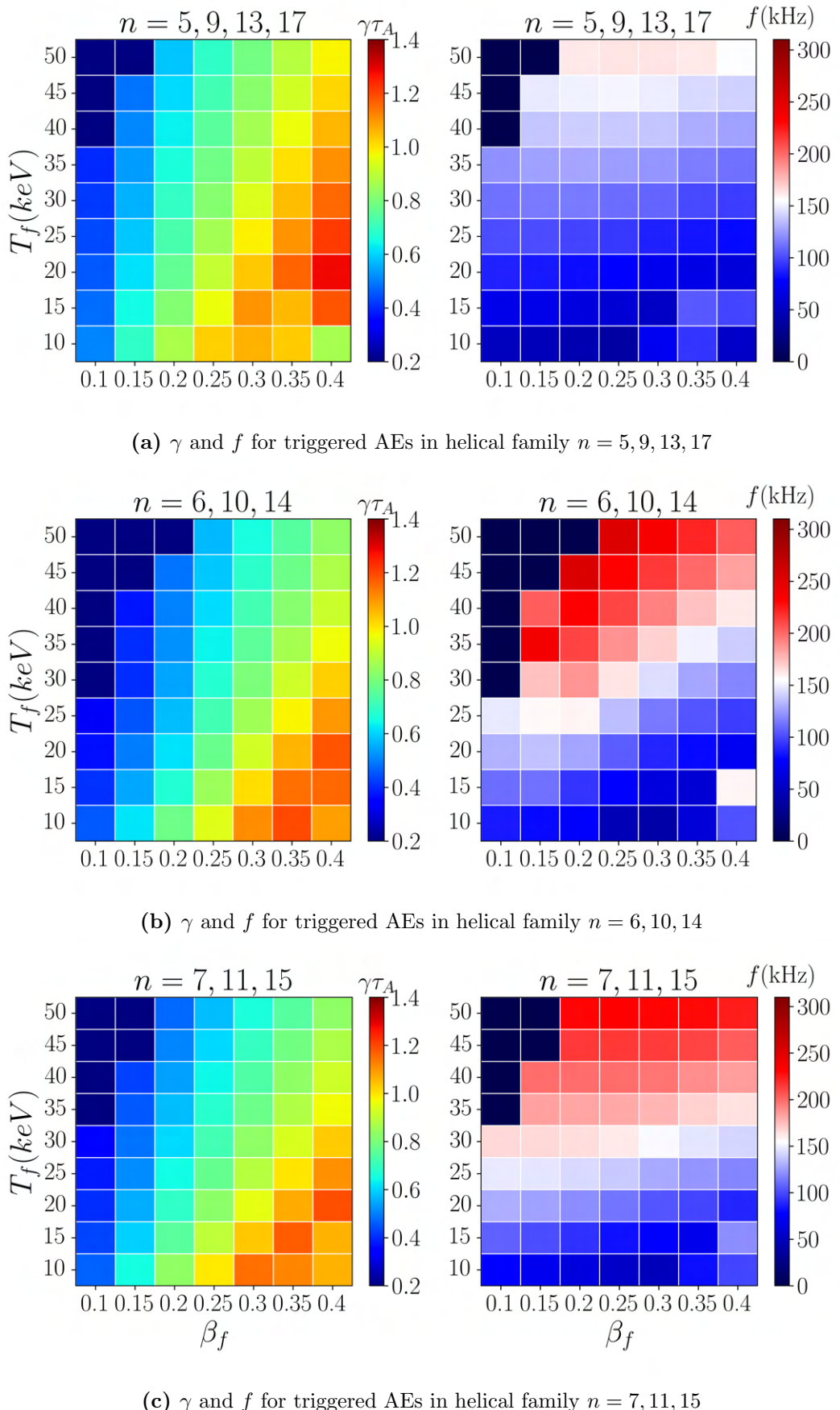
Figure 4.8 and 4.9 show the AE growth rate and frequency for different EP density profile gradients (see figure 3.6b), high and low gradient, respectively. Helical family  $n = 5, 9, 13, 17$ , high gradient (Figure 4.8a) is stable for  $\beta_f \leq 0.2$  and  $T_f \geq 40$ . For helical families  $n = 6, 10, 14$  and  $n = 7, 11, 15$  (Figure 4.8b and 4.8c respectively) **AE** stability is observed from EP energy of 35 keV to 50 keV and low beta values  $\beta_f \leq 0.2$ .

The simulations for the low EP density gradient case indicates the **AEs** are stable if the EP energy is  $T_f \geq 40$  keV and  $\beta_f \leq 0.15$ .

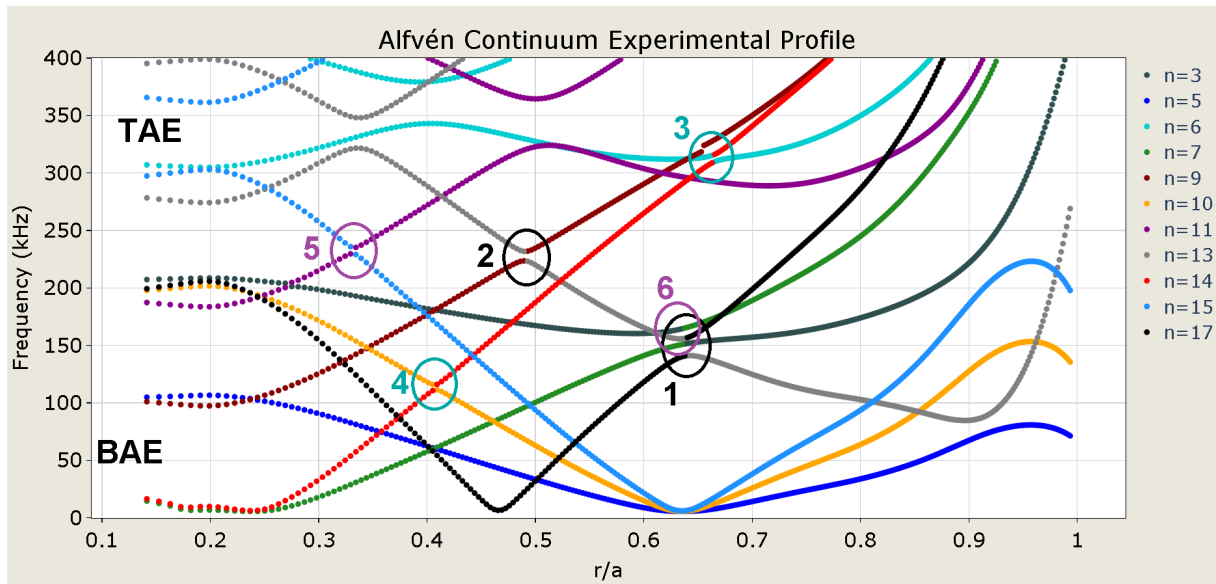
Figure 4.10 shows radial location and frequency range of the **AEs**. High gradient results are represented by a vertical line at the left, while low gradient profile have vertical line in the right side. Figure 4.10a shows **AEs** for helical family  $n = 5, 9, 13, 17$  are triggered around  $r/a = 0.31$  for high gradient case. If  $T_f = 15$  keV and  $\beta_f = 0.25 - 0.4$  **9/5 BAE** (figure 4.11a) is unstable. Although, **9/5 GAE** are trigger if  $T_f = 20$  keV. If  $T_f = 10$  keV and  $\beta_f = 0.35$  the **GAE 13/7** is trigger. Rest of parameters trigger **5/3 BAEs** and **GAEs**. For low gradient, average position is 0.61. If  $T_f = 10$  kev and  $\beta_f = 0.4$ , **17/10 BAE** (figure 4.11b) is unstable. The rest of values make **5/3 BAE** unstable. Helical family  $n = 6, 10, 14$ , average radial position is 0.28 for high gradient and 0.66 for low gradient profile. High gradient **6/3 BAE** and low gradient **6/4 BAE** are trigger at all EP energy values, however **14/8** is triggered by  $T_f = 10$  and  $\beta_f = 0.35 - 0.4$ . **10/6 BAE** is unstable if  $T_f = 15$  keV and  $\beta_f = 0.35 - 0.4$ . Low gradient **10/6 mode BAEs** is unstable if  $\beta_f \leq 0.25$  and  $T_f \leq 45$  keV.

Helical family  $n = 7, 11, 15$  is shown in Figure 4.10c. For high gradient case, average  $r/a = 0.34$ . **11/9 BAE** modes are unstable if  $T_f = 10 - 15$  keV  $\beta_f \geq 0.3$ . Middle plasma **AES** are unstable at  $r/a = 0.58$ . **15/9 BAEs** are trigger at  $\beta_f$  values 0.1, 0.35 and 0.4, and  $T_f \leq 15$  keV. If  $\beta_f = 0.4$  and  $T_f = 15$  kev, **11/7 BAE** is trigger.  $T_f \geq 35$  keV triggers **7/4 GAE**. Rest of parameters trigger **7/4 BAE**.

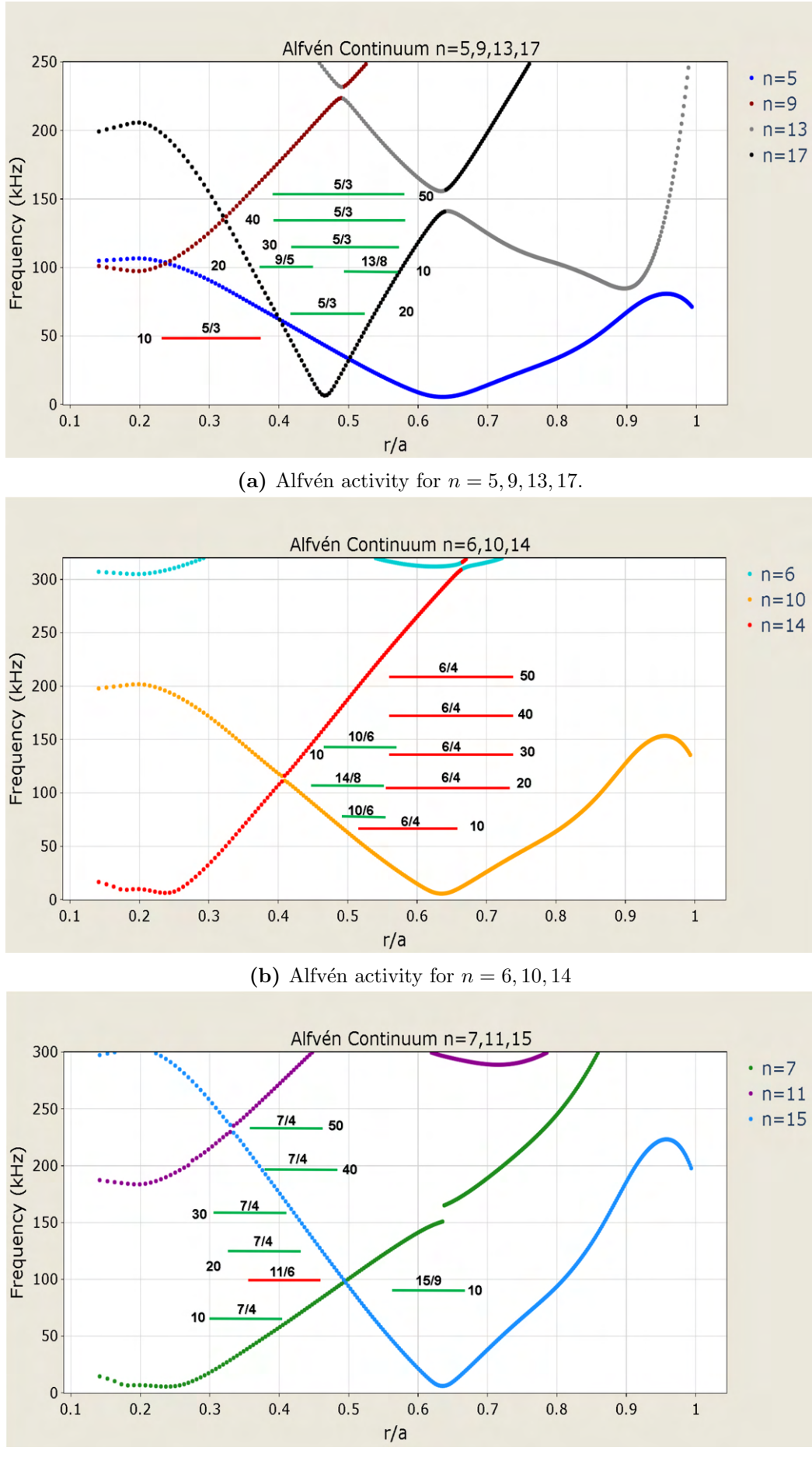
Presence of wider eigenfunctions at middle plasma radius are observed. Wide gaps between radial values of 0.5 and 0.8 allows destabilized **AES** to have higher growth rates. The fact that low gradient have low alfvénic stability is related to the fact that it's gradient region is positioned near middle plasma region, where gaps are large. In comparison to off-axis profile, gradient value have lower effect on **AES** stability.



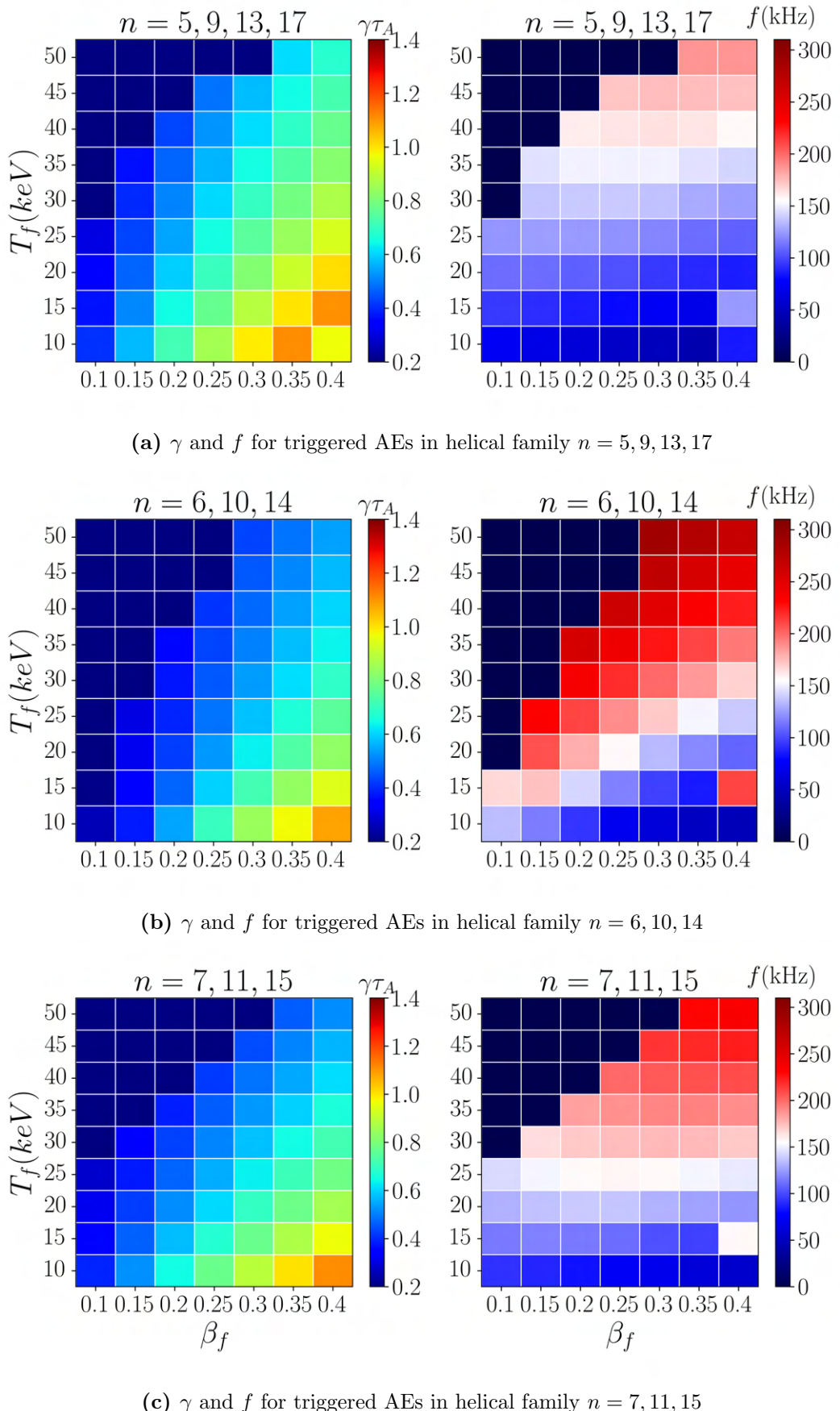
**Figure 4.1:** Heatmaps of growth rate (left) and frequency (right) of AE activity for the experimental profile.



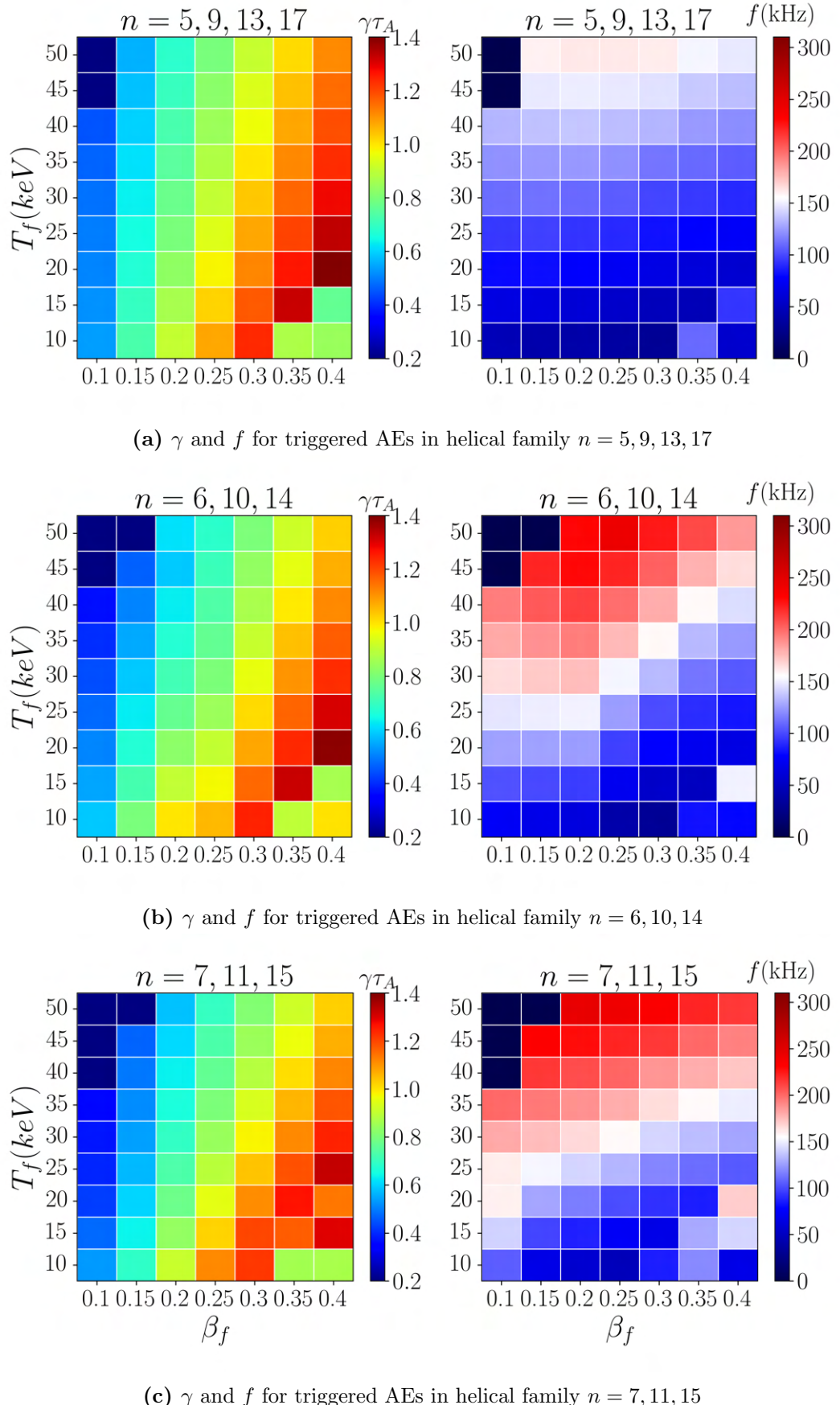
**Figure 4.2:** Alfvén continuum for experimental  $\iota$  calculated using *STELLGAP* code.



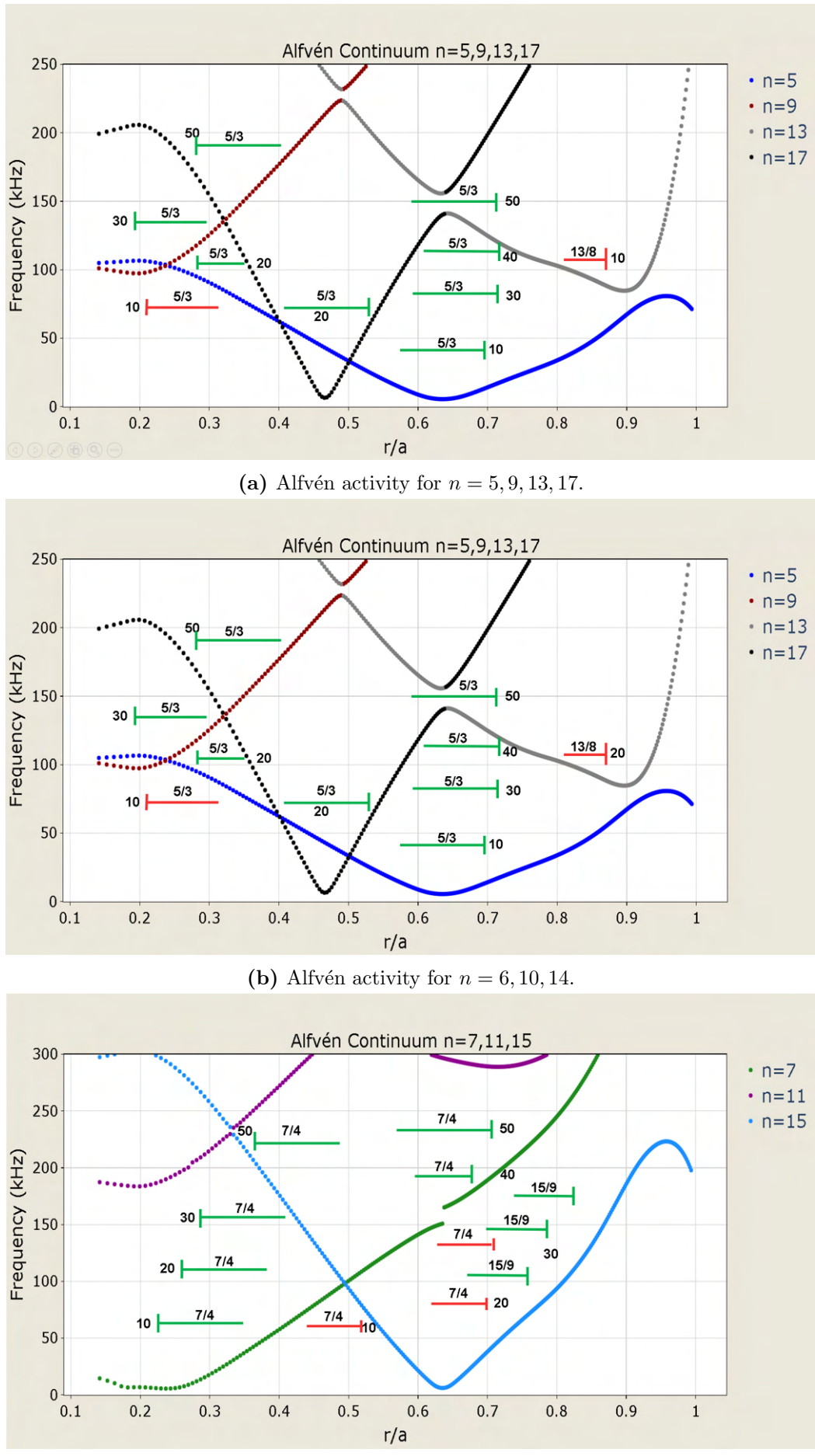
**Figure 4.3:** Alfvén activity for the experimental profiles.



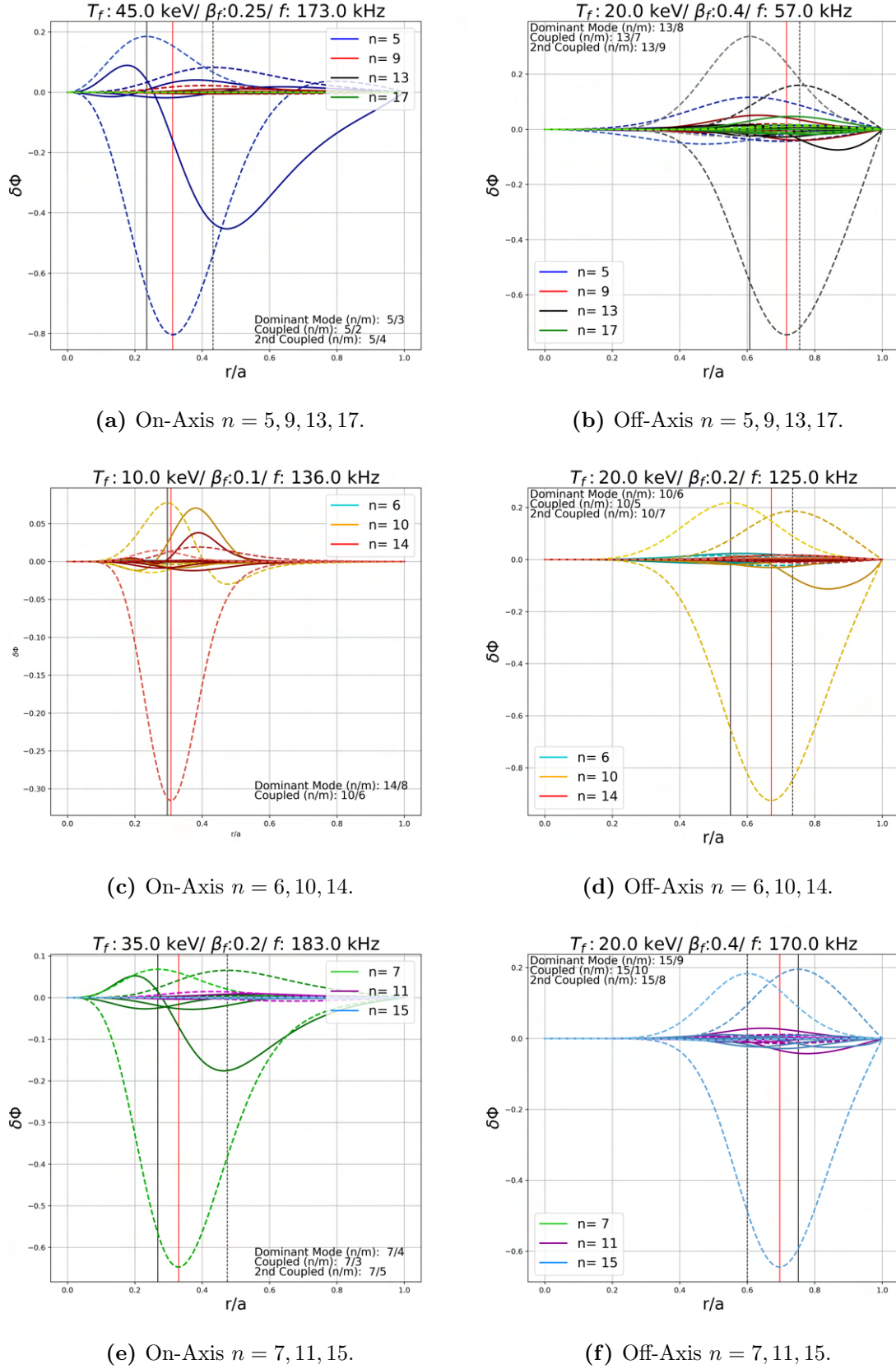
**Figure 4.4:** Heatmaps of growth rate (left) and frequency (right) of AE activity for on-axis profile.



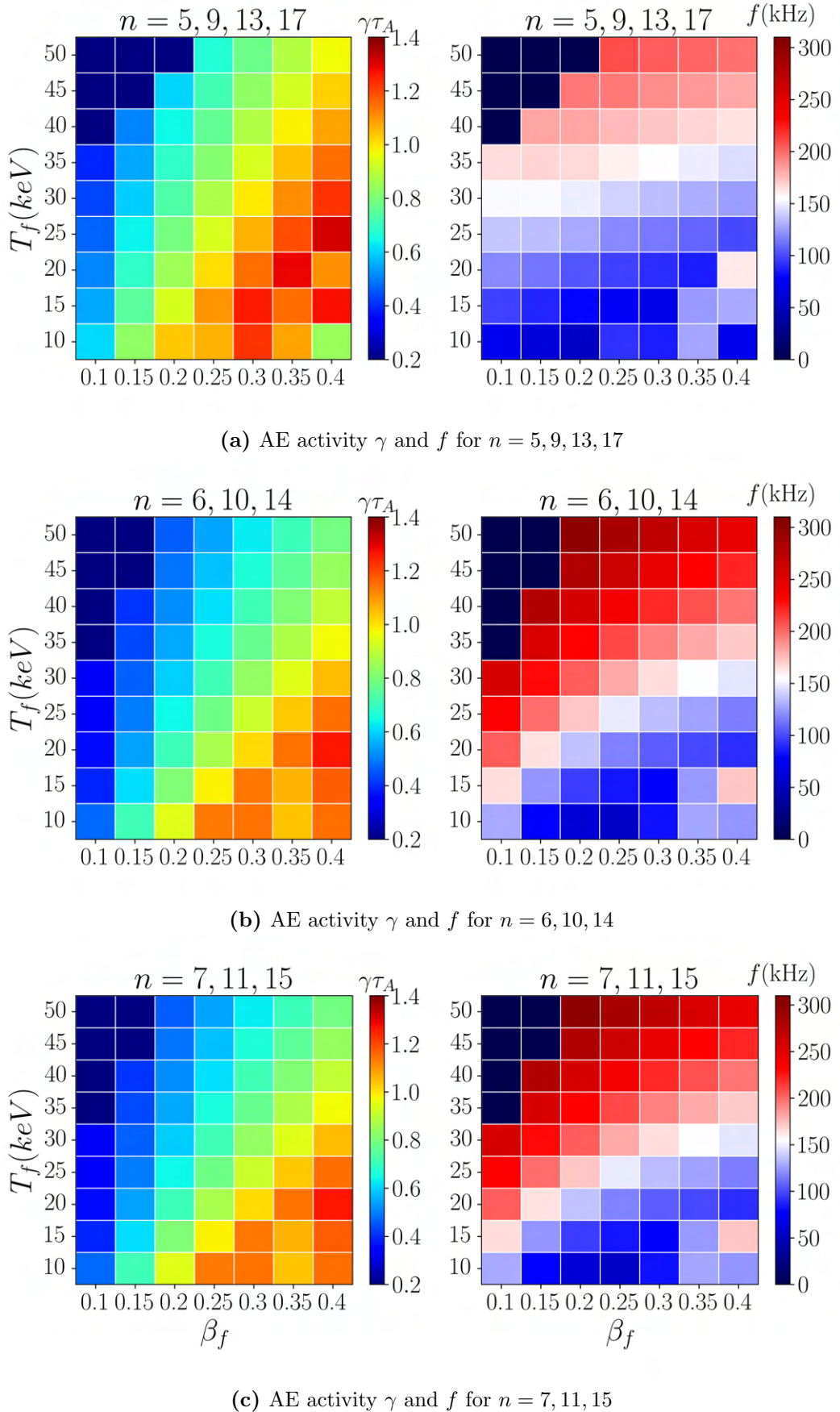
**Figure 4.5:** Heatmaps of growth rate (left) and frequency (right) of AE activity for Off-axis profile.



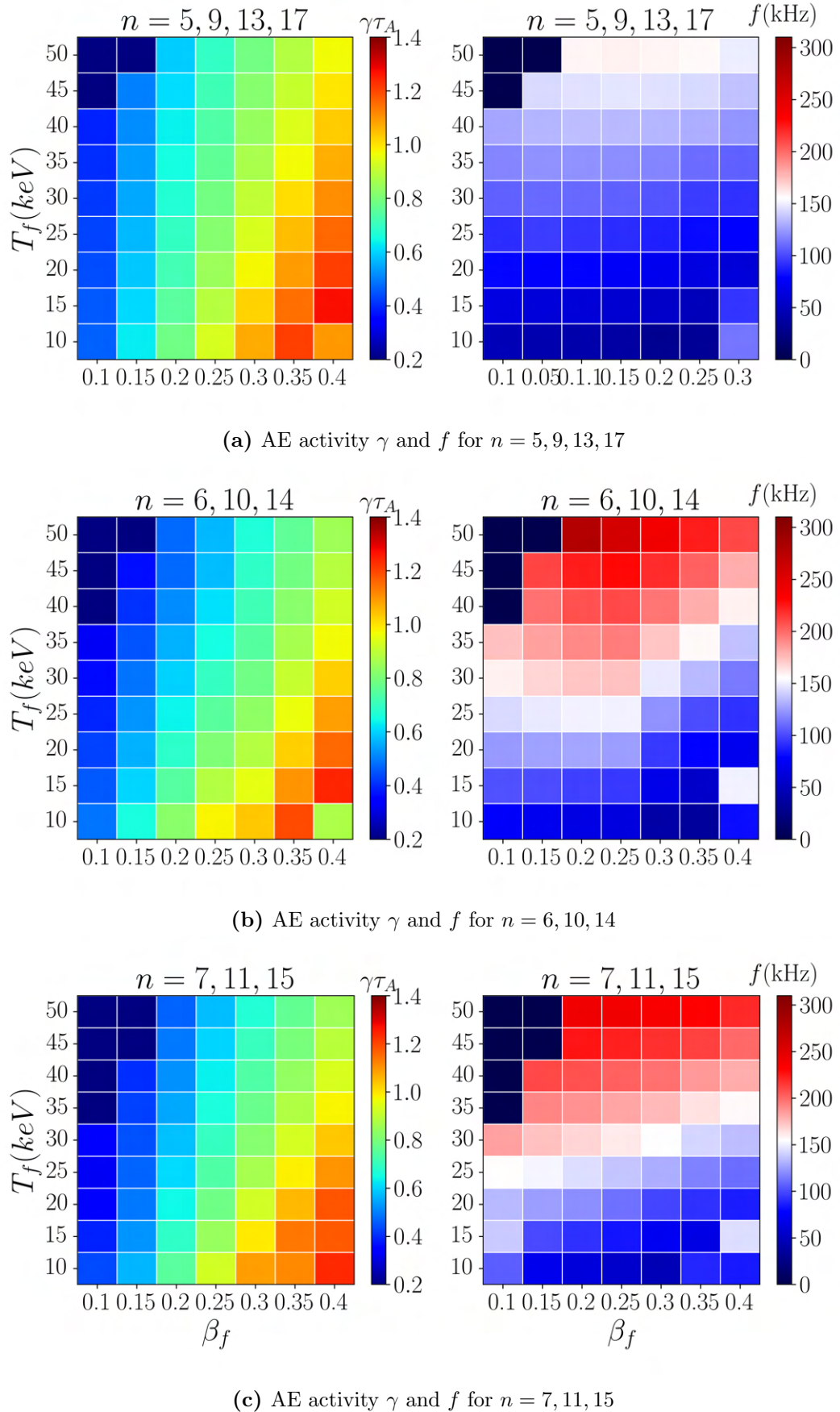
**Figure 4.6:** Alfvén activity for On-axis and Off-axis profile.



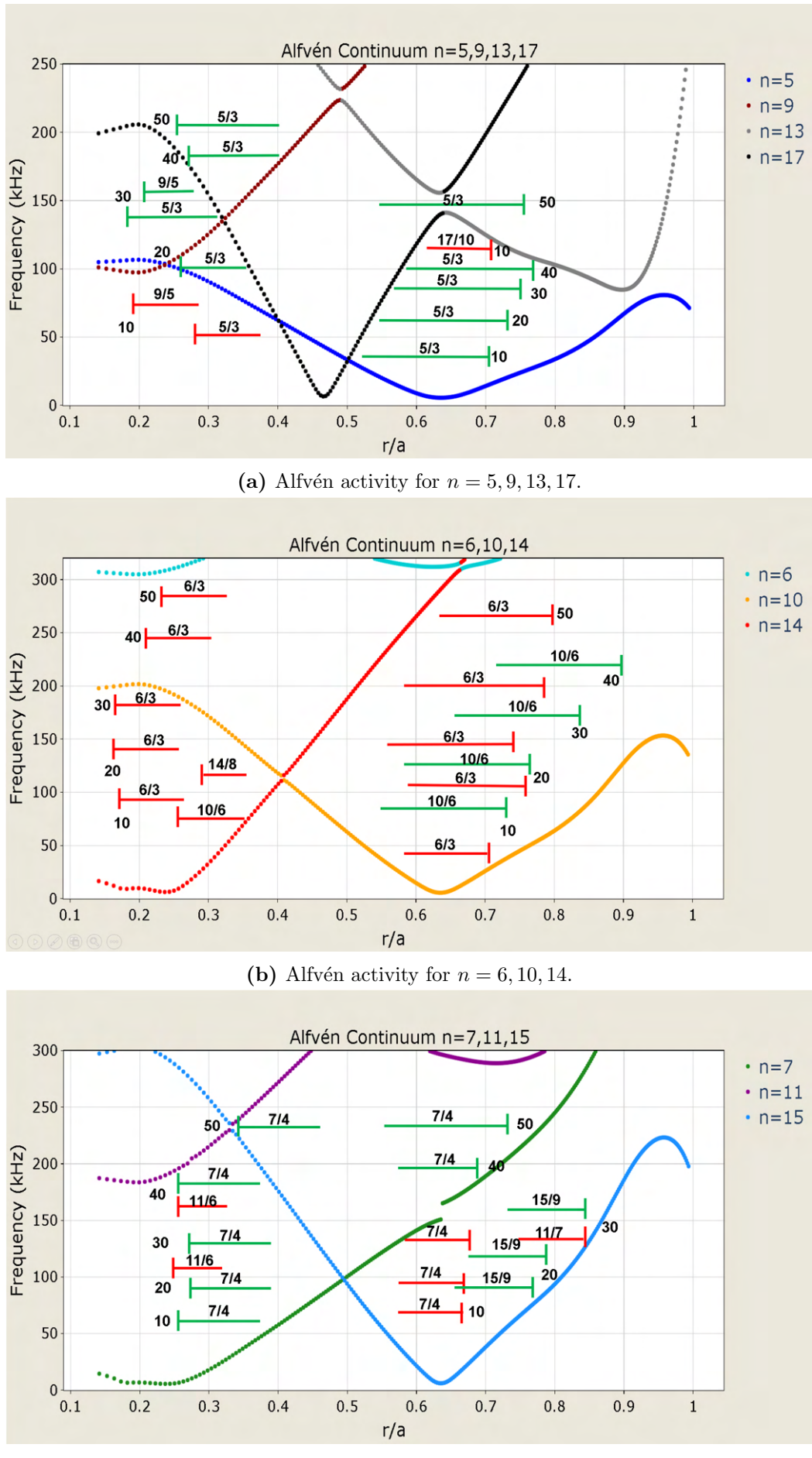
**Figure 4.7:** Electrostatic eigenfunctions for On-axis and Off-axis profile.



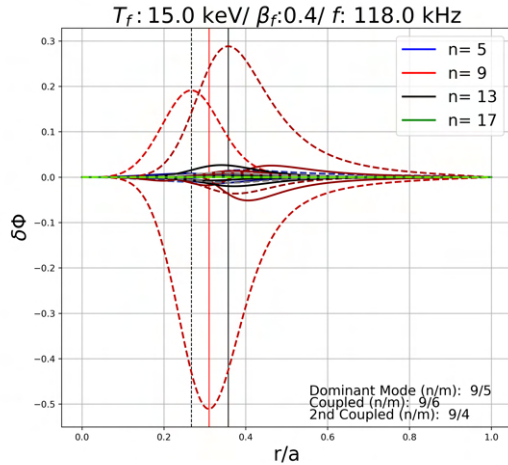
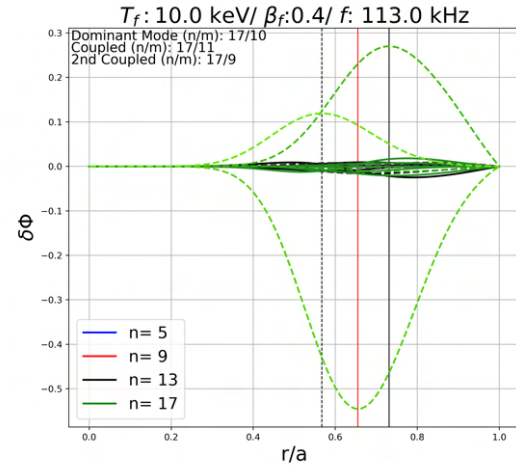
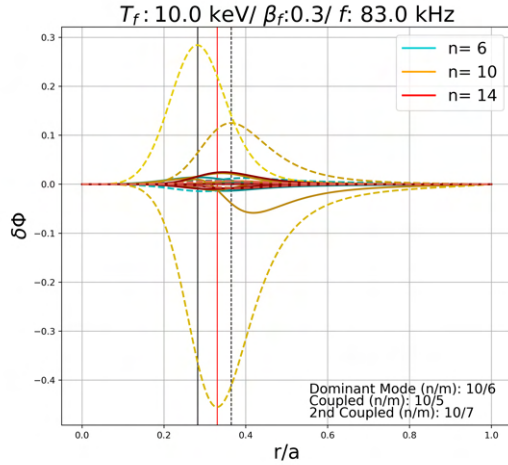
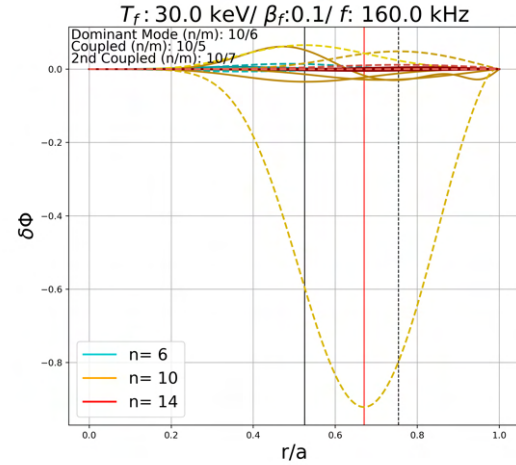
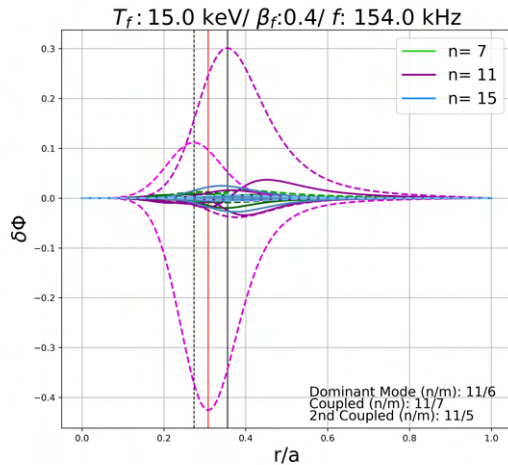
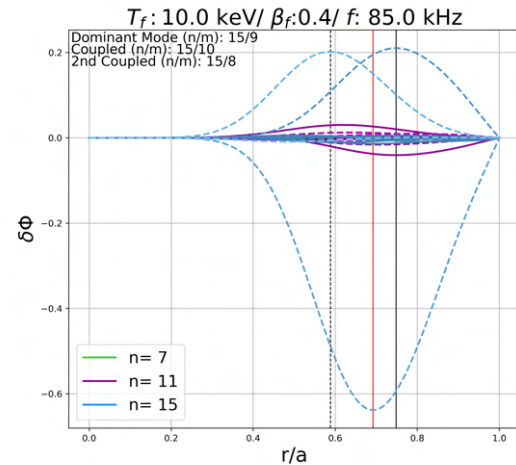
**Figure 4.8:** Growth rate (left) and frequency (right) of AE activity for high gradient profile.



**Figure 4.9:** Growth rate (left) and frequency (right) of AE activity for low gradient profile.



**Figure 4.10:** Alfvén activity in Alfvén continuum for high and low gradient profile.

(a) High-Gradient  $n = 5, 9, 13, 17$ .(b) Low-Gradient  $n = 5, 9, 13, 17$ .(c) High-Gradient  $n = 6, 10, 14$ .(d) Low-Gradient  $n = 6, 10, 14$ .(e) High-Gradient  $n = 7, 11, 15$ .(f) Low-Gradient  $n = 7, 11, 15$ .**Figure 4.11:** Electrostatic eigenfunctions for High and Low gradient profiles.

## 4.2 Magnetic Field Topology Variation

This section is dedicated to analyze the effect of the magnetic field configuration on the **AE** stability. The **AE** growth rate and frequency is shown in figure 4.12. In this figure, for each helical family results for  $\Delta\iota = -0.45$  are represented in purple dots,  $\Delta\iota = -0.25$  is in orange dots,  $\Delta\iota = 0.15$  are in red and in green dots  $\Delta\iota = 0.35$ .  $n = 5, 9, 13, 17$ , **AEs** are stable if  $\beta = 0.1$  from  $T_f = 40$  to 50 keV for  $\Delta\iota = -0.45$ . For  $\Delta\iota = -0.25$ , **AEs** are stable if  $T_f \geq 25$  keV and  $\beta \leq 0.25$ , for  $\Delta\iota = 0.15$   $T_f \geq 20$  keV and  $\beta \leq 0.35$  and for  $\Delta\iota = 0.35$  if  $\beta \leq 0.3$  and  $T_f \geq 25$  keV.

The study of helical family  $n = 6, 10, 14$  (Figure 4.12c and 4.12d) shows stable **AEs** if  $\beta_f \leq 0.15$  and  $T_f \geq 45$  keV for  $\Delta\iota = -0.45$  and  $\Delta\iota = -0.25$ .  $\Delta\iota = 0.15$  is stable if  $T_f \geq 20$  keV and  $\beta_f \leq 0.35$ .  $\Delta\iota = 0.35$  shows stability if  $T_f \geq 15$  keV and  $\beta_f \leq 0.35$ .

Results for helical family  $n = 7, 11, 15$  are presented in figures 4.12e and 4.12f. For this family,  $\Delta\iota = 0.35$  shows stable **AEs** for all parameters studied. Concerning  $\Delta\iota = -0.45$ , **AE** are stable if  $T_f \geq 35$  keV and  $\beta_f \leq 0.3$ .  $\Delta\iota = -0.25$  is stable if  $T_f \geq 35$  keV and  $\beta_f \leq 0.35$ , and  $\Delta\iota = 0.15$  shows stability if  $T_f \geq 25$  keV and  $\beta_f \leq 0.3$ .

Figure 4.13 shows the Alfvén Continuum for the different magnetic field configurations. **TAE** and **BAE** gaps are marked in the figures. Table 4.1 states the helical coupling modes that creates the **HAE** gaps on the Alfvén Continuum for the configurations. Label colors in figure 4.13 are the same as in figure 4.2.

Results for the helical family  $n = 5, 9, 13, 17$  **AEs** are shown in Figure 4.14.  $\Delta\iota = -0.45$  (Figure 4.14a),  $\Delta\iota = -0.25$  (Figure 4.14b) and  $\Delta\iota = 0.15$  (Figure 4.14c). Simulations show for this configurations **AEs** are triggered near the plasma core and higher modes are trigger for  $T_f \geq 30$  keV.  $\Delta\iota = 0.35$  (Figure 4.14d) moves the **AEs** towards the periphery as  $T_f$  increases.

Alfvén activity for  $n = 6, 10, 14$  is shown in Figure 4.15.  $\Delta\iota = 0.35$  (Figure 4.15d) **AEs** are triggered at the plasma core.  $\Delta\iota = -0.45$ , shown in Figure 4.15a), moves the **AEs** towards the core as the  $T_f$  increases.  $\Delta\iota = -0.25$  is shown in Figure 4.15b) and  $\Delta\iota = 0.15$  in Figure 4.15c.  $\Delta\iota = -0.45$  and  $\Delta\iota = 0.35$  shows transition from **BAE** to **GAE** at  $T_f = 20$  keV.  $\Delta\iota = -0.25$  and  $\Delta\iota = 0.15$  shows transition from **BAE** to **GAE** at  $T_f = 30$  keV.

Alfvén activity for  $n = 7, 11, 15$  is shown in Figure 4.16.  $\Delta\iota = -0.45$  shown in Figure 4.16a), presents transition from **BAE** to **GAE** at  $T_f \geq 30$  keV.  $\Delta\iota = -0.25$  is shonw in Figure 4.16b. If  $T_f = 20$  keV,  $n/m = 3/2$  **GAE** are trigger at the plasma core.  $\Delta\iota = 0.15$  is in Figure 4.16c) where transition between **BAE** to **GAE** is observed if  $T_f \geq 40$  keV.

**Table 4.1:** **HAE** gaps for different Magnetic Topology configurations.

	-0.45	-0.25	0.15	0.35
1	$n = 5, 9$	$n = 7, 11$	$n = 13, 15$	–
2	$n = 11, 15$	$n = 3, 7$	$n = 9, 13$	–
3	–	$n = 13, 17$	$n = 5, 13$	–
4	–	–	$n = 10, 14$	–
5	–	–	$n = 11, 15$	–
6	–	–	$n = 7, 11$	–

Lower iota profile shows the destabilization of low  $n$  modes ( $n/m = 5/4, 5/3$ ). However, positive  $\iota$  displacement show the destabilization of higher  $n$  modes compared to lower iota configurations. The configuration with higher iota shows the lowest growth rate (case with  $\Delta\iota = 0.35$ ). For this configuration helical family  $n = 7, 11, 15$  is stable for all parameters and helical families.  $n = 5, 9, 13, 17$  and  $n = 6, 10, 14$  are stable if  $T_f \geq 15$  keV and  $\beta_f \leq 0.35$  showing the lowest growth rates.

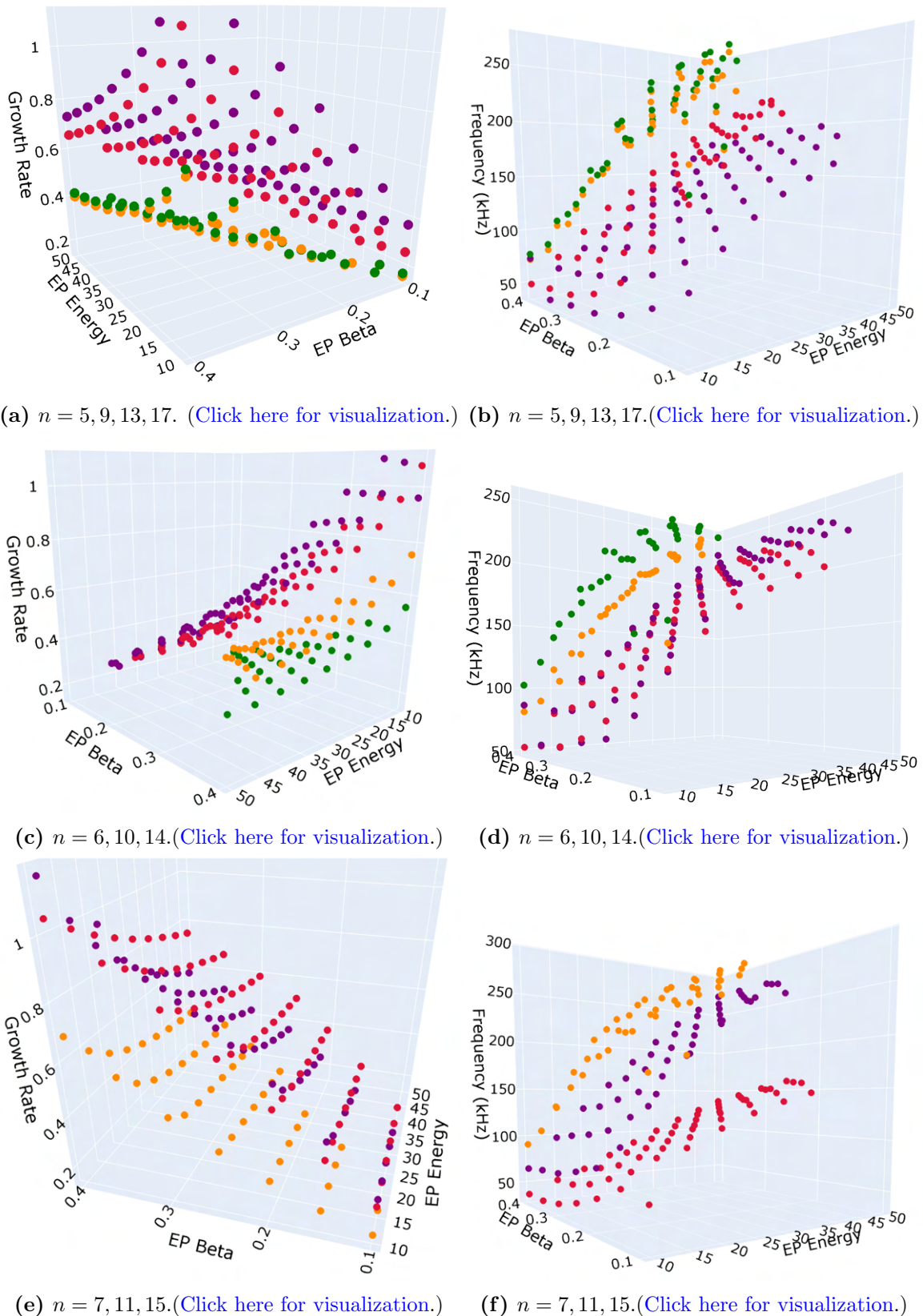


**Figure 4.12:** Magnetic topology study of growth rate (left) and frequency (right). In purple  $\Delta\iota = -0.45$ , in orange  $\Delta\iota = -0.25$ , in red  $\Delta\iota = 0.15$ , in green  $\Delta\iota = 0.35$

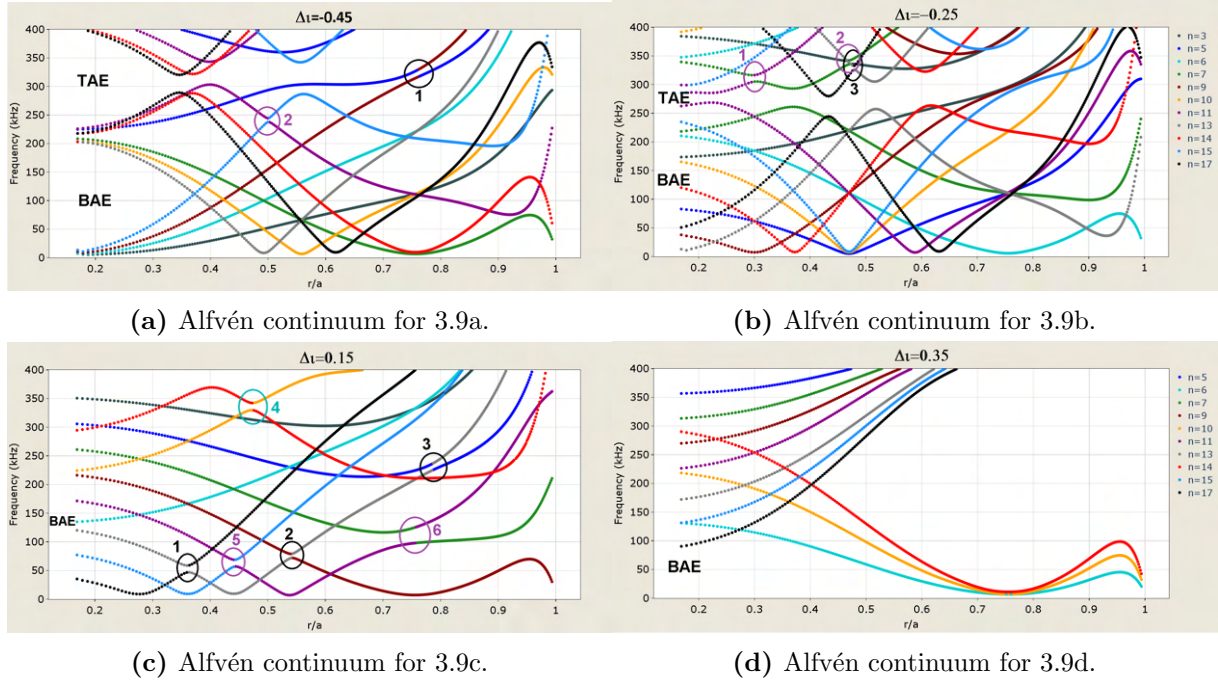


**Figure 4.13:**  $\Delta t$  Alfvén Continuum for the study of magnetic topology variations.

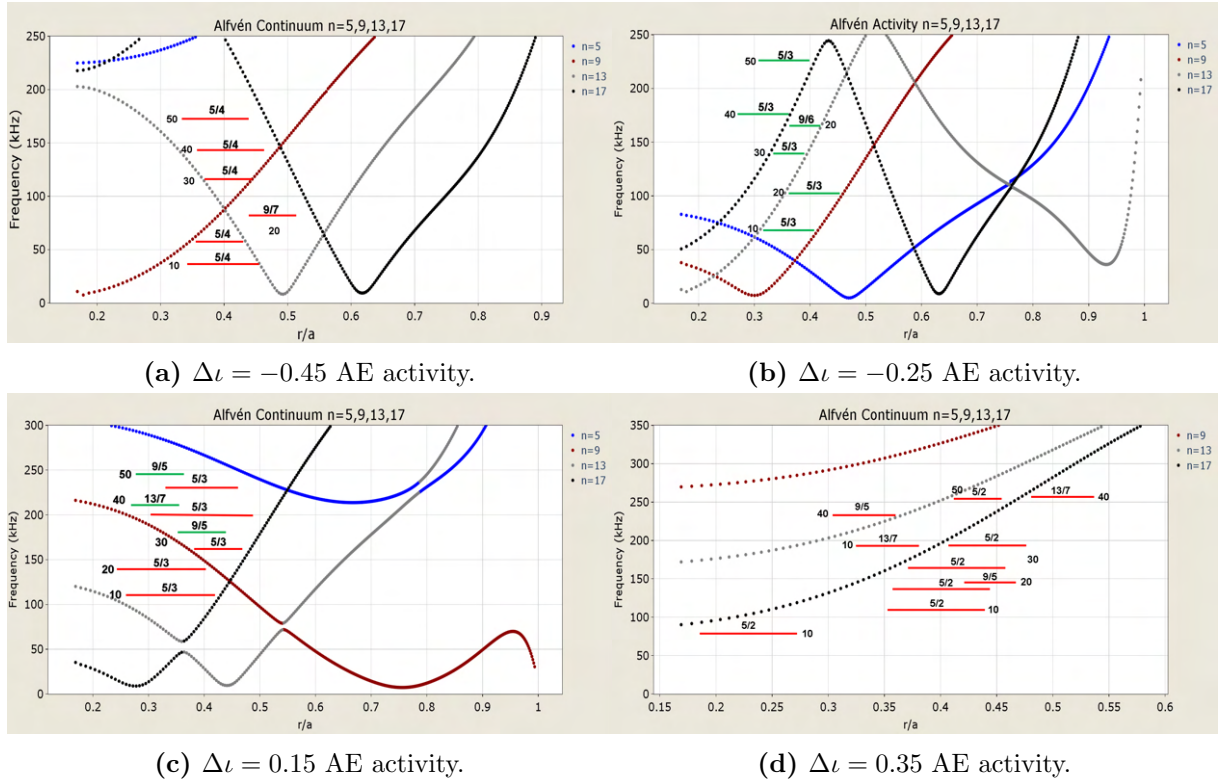


**Figure 4.14:**  $n = 5, 9, 13, 17$  Alfvén activity for rotational transform profiles.

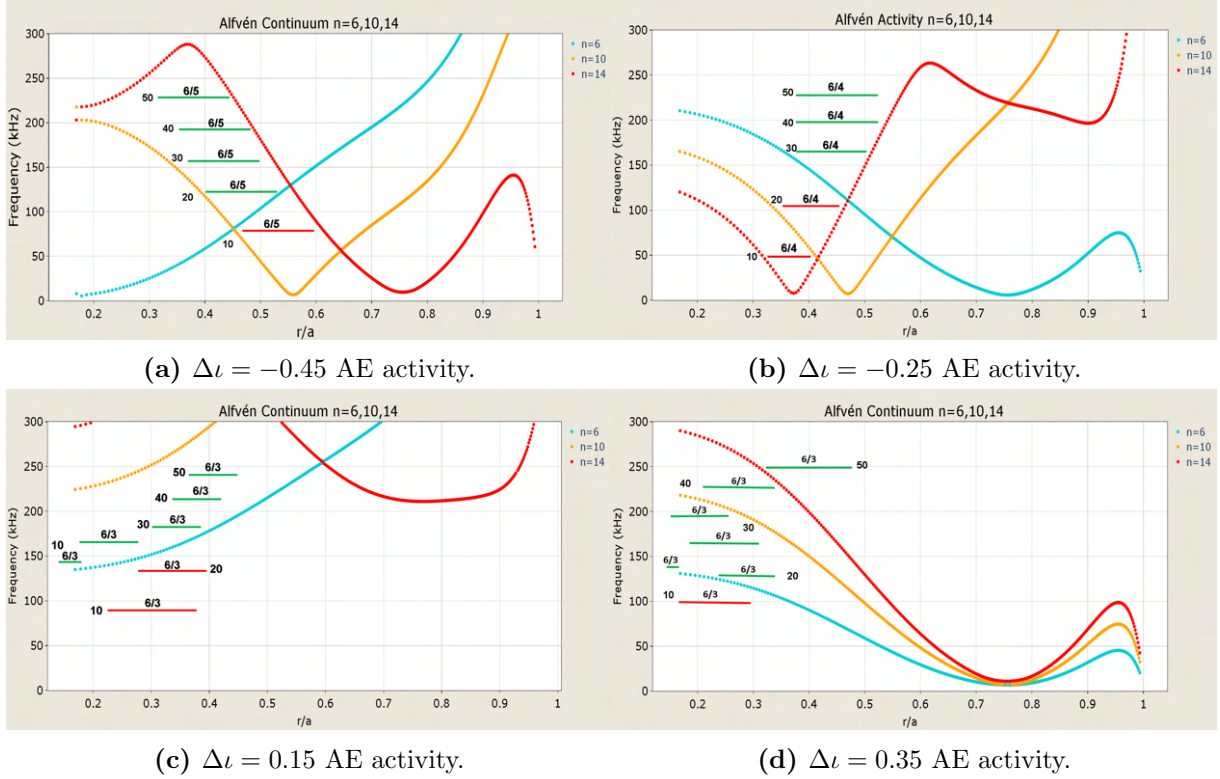


**Figure 4.15:**  $n = 6, 10, 14$  Alfvén activity for rotational transform profiles.

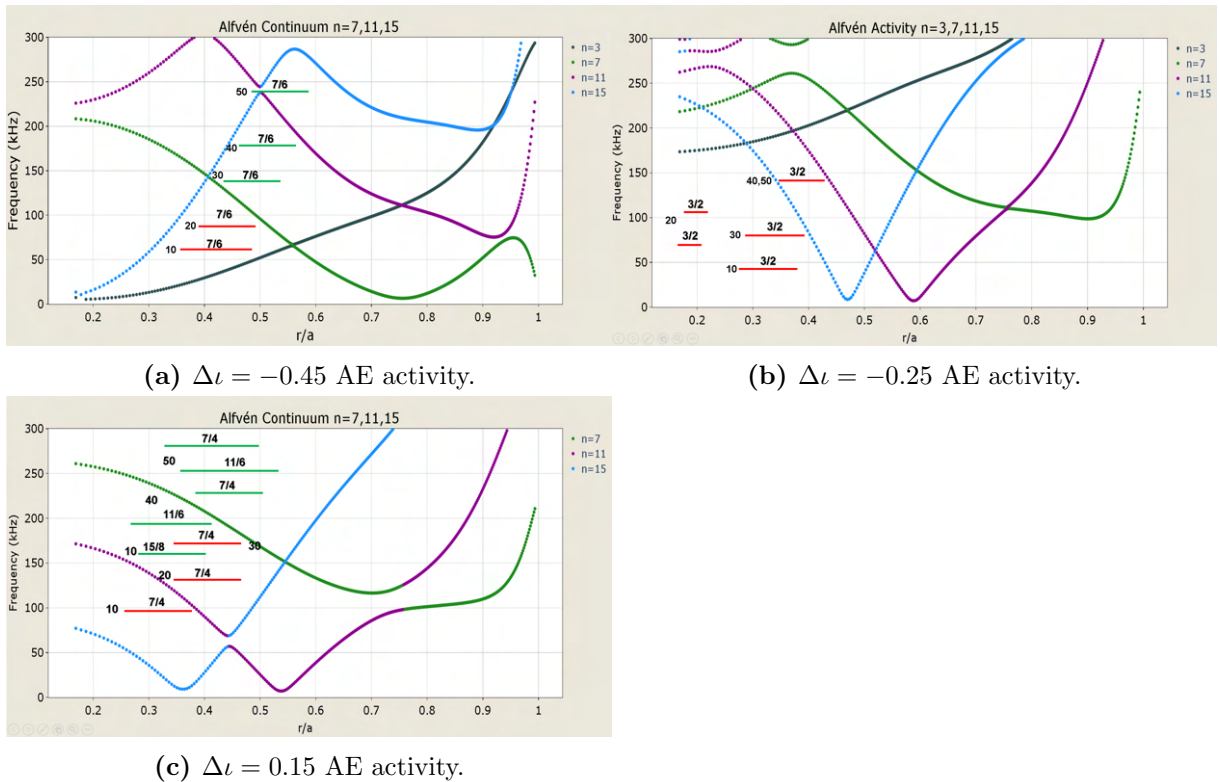


**Figure 4.16:**  $n = 7, 11, 15$  Alfvén activity for rotational transform profiles.



# Chapter 5

## Discussion

### 5.0.1 Optimization of the NBI Operational Regime

The analysis of the **AE** stability with respect to the NBI deposition region shows that on-axis profile presents improvement in **AE** stability. Off-axis NBI configurations leads to the injection of **EPs** in a plasma region where the gaps in the continuum are larger, allowing **AEs** to grow for lower  $\beta_f$  and  $T_f$ . Recommended optimal operation for NBI is at  $T_f = 50\text{keV}$  where critical  $\beta_f$  is 0.3 for On-axis profile. If  $\beta_f \geq 0.3$ , 5/3,6/4 and 7/4 **GAEs** are unstable.

The study of gradient variation shows a lower EP beta to trigger **AEs** in the high **EP** density gradient case. Also, eigenfunctions are narrower. However,  $\gamma_s$  are larger. Low gradient **EP** density configuration shows lower growth rates. If the  $\beta_f \geq 0.2$ , 5/3, 7/4 **GAEs** and 6/4**BAEs** are destabilized.

Off-axis profile shows the largest **AEs** instabilities growth rate between the cases analyzed. Finally, the optimum configuration NBI deposition as well as a large spreading of the beam to reduce the **EP** density gradients, avoiding the destabilization of **AEs** with large growth rates.

### 5.0.2 Magnetic Topology Alfvén Eigenmodes Optimization

All the iota profiles studied show a lower **AE** growth rate and destabilization of **AEs** with respect to reference case.

The configuration leading to the optimal **AE** is observed for an increase of the iota profile by  $\Delta\iota = 0.35$ . If the  $\beta_f \geq 0.35$  and  $T_f = 50 \text{ keV}$ , 5/3 and 6/3 **GAEs** are triggered. This configuration shows the minimum amount of resonant modes between all configurations. Nevertheless, off-axis NBI operation should be avoided in this configuration because wide gaps exist in the middle-outer plasma region.

**AEs** are trigger in the plasma core for  $\Delta\iota = -0.25, 0.15$  configurations, although the **AE** are main located in middle plasma for  $\Delta\iota = -0.45, 0.35$  configurations. All the configurations analyzed shows dominant  $n = 5, 6$  and  $7$ , except for the  $\Delta\iota = -0.25$  configuration showing dominant  $n=3$  **AEs**.

Summarizing, the optimal operations of TJ-II stellarator to improve the AE stability concerning magnetic trap requires a rotational transform between [1.975,2.1].



# Chapter 6

## Conclusions and Future Work

The **AE** stability in TJ-II plasma is analyzed with respect to the NBI operational regime and the magnetic field configuration.  $\beta_f$  shows to have an impact in increasing growth rate for unstable **AEs**. Higher  $T_f$  have the effect of destabilize higher frequency **AEs**. Parametric studies are useful to identify optimized operational regimes with respect to the **AE** stability, required to improve the plasma heating and performance of future fusion reactors.

**AEs** stability is improved for on-axis NBI injection and low gradient **EP** density profiles (large beam spreading). Such NBI operational regime leads to an  $\beta_f$  threshold for the **AE** destabilization of 0.35 if  $T_f = 50$  keV.

The analysis of the magnetic field configuration indicates that an increment of the iota profile by  $\Delta\iota = 0.35$  lead to an improvement of the **AE** stability.

Addition of damping effects like electron-ion Landau damping and thermal plasma finite Larmour radius effects are proposed for improvements to this work. For future analyzes, the eigensolver module of *FAR3d* may add more information on sub-dominant modes. Non-linear studies should be conducted to study the saturation phase of the **AEs** and the **EP** transport induced. Similar studies for the purpose of **AE** stability optimization may be conducted in other devices.

Furthermore, optimization of the acquisition and analysis software developed for this work is in progress.

In conclusion, optimization study objectives have been achieved. Linear simulations results with *FAR3d* code have been presented. Results show that this analyzes are required to improve the performance of future nuclear fusion devices.



# Bibliography

- [1] W. M. Stacey. *Fusion plasma physics*. John Wiley & Sons, 2012
- [2] S. E. Wurzel and S. C. Hsu. Progress toward fusion energy breakeven and gain as measured against the Lawson criterion. *Physics of Plasmas*, **29** (2022) (6) 062103
- [3] J. P. Freidberg. Magnetic Fusion Confinement with Tokamaks and Stellarators. *IAEA Bulletin*, **60** (2019) (3) 28–33
- [4] S. Sharapov, B. Alper, H. Berk, D. Borba, B. Breizman, C. Challis, I. Classen, E. Edlund, J. Eriksson, A. Fasoli, et al. Energetic particle instabilities in fusion plasmas. *Nuclear Fusion*, **53** (2013) (10) 104022
- [5] S. Mulas, Á. Cappa, J. Kontula, D. López-Bruna, I. Calvo, F. Parra, M. Liniers, T. Kurki-Suonio, and M. Mantsinen. ASCOT5 simulations of neutral beam heating and current drive in the TJ-II stellarator. *Nuclear Fusion*, **62** (2022) (10) 106008
- [6] G. Simon da Rosa, J. Bergmann, and F. Teixeira. A Perturbation Method to Model Electromagnetic Well-Logging Tools in Curved Boreholes. *IEEE Transactions on Geoscience and Remote Sensing*, **PP** (2017) 1–15. URL <http://dx.doi.org/10.1109/TGRS.2017.2771723>
- [7] W. Heidbrink. Basic physics of Alfvén instabilities driven by energetic particles in toroidally confined plasmas. *Physics of Plasmas*, **15** (2008) (5) 055501
- [8] J. Varela, A. Shimizu, D. Spong, L. Garcia, and Y. Ghai. Study of the Alfvén eigenmodes stability in CFQS plasma using a Landau closure model. *Nuclear Fusion*, **61** (2021) (2) 026023
- [9] M. Gordon and M. Weber. Global energy demand to grow 47% by 2050, with oil still top source: US EIA. Available from: <https://www.spglobal.com/commodityinsights/en/market-insights/latest-news/oil/100621-global-energy-demand-to-grow-47-by-2050-with-oil-still-top-source-us-eia>, 2021
- [10] International Energy Agency. Outlook for energy demand. <https://www.iea.org/reports/world-energy-outlook-2022/outlook-for-energy-demand>, 2022
- [11] E. E. El-Hinnawi. Review of the environmental impact of nuclear energy. (1977)
- [12] F. Barbir, T. Veziroğlu, and H. Plass Jr. Environmental damage due to fossil fuels use. *International journal of hydrogen energy*, **15** (1990) (10) 739–749
- [13] K. Hari. Energy crisis and nuclear fusion power. *Himalayan Physics*, **5** (2014) 131–136

- [14] M. Alwaeli and V. Mannheim. Investigation into the current state of nuclear energy and nuclear waste management—A state-of-the-art review. *Energies*, **15** (2022) (12) 4275
- [15] J. D. Lawson. Some criteria for a power producing thermonuclear reactor. *Proceedings of the physical society. Section B*, **70** (1957) (1) 6
- [16] K. Nishikawa and M. Wakatani. *Plasma physics*, volume 8. Springer Science & Business Media, 2000
- [17] S. Pinches, H. Berk, D. Borba, B. Breizman, S. Briguglio, A. Fasoli, G. Fogaccia, M. Gryaznevich, V. Kiptily, M. Mantsinen, et al. The role of energetic particles in fusion plasmas. *Plasma physics and controlled fusion*, **46** (2004) (12B) B187
- [18] C. Wei and W. Zheng-Xiong. Energetic particles in magnetic confinement fusion plasmas. *Chinese Physics Letters*, **37** (2020) (12) 125001
- [19] K.-L. Wong. A review of Alfvén eigenmode observations in toroidal plasmas. *Plasma physics and controlled fusion*, **41** (1999) (1) R1
- [20] K. Toi, F. Watanabe, T. Tokuzawa, K. Ida, S. Morita, T. Ido, A. Shimizu, M. Isobe, K. Ogawa, D. A. Spong, et al. Observation of reversed-shear Alfvén eigenmodes excited by energetic ions in a helical plasma. *Physical review letters*, **105** (2010) (14) 145003
- [21] M. Osakabe, S. Yamamoto, K. Toi, Y. Takeiri, S. Sakakibara, K. Nagaoka, K. Tanaka, K. Narihara, L. E. Group, et al. Experimental observations of enhanced radial transport of energetic particles with Alfvén eigenmode on the LHD. *Nuclear fusion*, **46** (2006) (10) S911
- [22] N. N. Gorelenkov, S. Pinches, and K. Toi. Energetic particle physics in fusion research in preparation for burning plasma experiments. *Nuclear Fusion*, **54** (2014) (12) 125001
- [23] C. Hidalgo, E. Ascasíbar, D. Alegre, A. Alonso, J. Alonso, R. Antón, A. Baciero, J. Baldzuhn, J. Barcala, L. Barrera, et al. Overview of the TJ-II stellarator research programme towards model validation in fusion plasmas. *Nuclear Fusion*, **62** (2022) (4) 042025
- [24] D. Hartmann. Stellarators. *Fusion science and technology*, **57** (2010) (2T) 46–58
- [25] D. Rapisarda, B. Zurro, and A. Baciero. First Toroidal Rotation Measurements of Protons and Impurities in the TJ-II Stellarator; Primeras Medidas de Rotacion Toroidal de Protones e Impurezas en el Stellarator TJ-II. (2006)
- [26] B. Zurro, A. Baciero, V. Tribaldos, M. Liniers, A. Cappa, A. Lopez-Fraguas, D. Jimenez-Rey, J. Fontdecaba, O. Nekhaieva, et al. Suprathermal ion studies in ECRH and NBI phases of the TJ-II stellarator. *Nuclear Fusion*, **53** (2013) (8) 083017
- [27] Á. Cappa, J. Varela, D. L. Bruna, E. Ascasíbar, M. Liniers, L. Eliseev, J. Fontdecaba, J. García-Regaña, A. González-Jerez, N. Kharchev, et al. Stability analysis of TJ-II stellarator NBI driven Alfvén eigenmodes in ECRH and ECCD experiments. *Nuclear Fusion*, **61** (2021) (6) 066019

- [28] A. Melnikov, L. Eliseev, E. Ascasibar, A. Chmyga, C. Hidalgo, T. Ido, R. Jiménez-Gómez, A. Komarov, A. Kozachek, L. Krupnik, et al. Alfvén eigenmode properties and dynamics in the TJ-II stellarator. *Nuclear Fusion*, **52** (2012) (12) 123004
- [29] J. P. Freidberg. *ideal MHD*. Cambridge University Press, 2014
- [30] D. A. Spong, R. Sanchez, and A. Weller. Shear Alfvén continua in stellarators. *Physics of Plasmas*, **10** (2003) (8) 3217–3224
- [31] E. Belova, E. Fredrickson, J. Lestz, N. Crocker, and N.-U. Team. Numerical simulations of global Alfvén eigenmodes excitation and stabilization in NSTX-U. *Physics of Plasmas*, **26** (2019) (9) 092507
- [32] W. Heidbrink, E. Ruskov, E. Carolipio, J. Fang, M. Van Zeeland, and R. James. What is the “beta-induced Alfvén eigenmode?”. *Physics of Plasmas*, **6** (1999) (4) 1147–1161
- [33] R. Betti and J. Freidberg. Ellipticity induced Alfvén eigenmodes. *Physics of Fluids B: Plasma Physics*, **3** (1991) (8) 1865–1870
- [34] J. Varela, D. Spong, and L. Garcia. Analysis of Alfvén eigenmode destabilization by energetic particles in Large Helical Device using a Landau-closure model. *Nuclear Fusion*, **57** (2017) (4) 046018
- [35] D. A. Spong. Simulation of Alfvén frequency cascade modes in reversed shear-discharges using a Landau-closure model. *Nuclear Fusion*, **53** (2013) (5) 053008
- [36] D. Dixon, T. Marshall, and A. Sen. Effects of finite Larmor radius and ion Landau damping on the dissipative trapped electron instability. *Plasma Physics*, **20** (1978) (3) 189
- [37] D. Spong, L. Garcia, J. Varela, and Y. Ghai. *FAR3d code: User’s Guide*. Oak Ridge National Laboratory, Tennessee, 1 edition, 2020
- [38] J. Varela, D. A. Spong, and L. Garcia. Analysis of Alfvén eigenmodes destabilization by energetic particles in TJ-II using a Landau-closure model. *Nuclear Fusion*, **57** (2017) (12) 126019
- [39] J. Ortiz, J. Varela, D. Spong, L. Garcia, and Y. Ghai. Study of the Alfvén Eigenmodes stability in Quasi Poloidal Stellarator (QPS) plasma using a Landau closure model. *Nuclear Fusion*, **63** (2023) (5) 13



# **Appendix A**

## **Nomenclature**

**Table A.1:** Variables used in the *FAR3d* code.

Symbol	Name	Normalization
$\rho$	Generalized radial coordinate	$\rho/a$
B	Magnetic Field	$B/B_0$
$\tilde{p}$	Plasma pressure	$P/P_0$
$\Phi$	Electrostatic Potential	$\tau_{A0}\Phi/aB_0]$
$\Psi$	Magnetic flux	$a^2B_0$
S	Lundqvist number	
$v_{  ,th}$	Thermal particles parallel velocity	
$n_f$	Energetic particle density	$n_f/n_0$
$v_{th,f}$	Energetic particle thermal velocity	
$\omega_{cy,f}$	Energetic particles cyclotron frequency	$\omega_{cy,f}\tau_{A0}$
$q_f$	Energetic particle charge	
$R_{L,f}$	Finite Larmour Radius	$R_{L,f}/a$
$T_f$	Energetic particle energy	

# Acknowledgements

I would like to start giving my deepest gratitude to my thesis supervisor Jacobo Varela, who have been supportive during the whole project and have shared his extensive expertise, allowing me to learn beyond the limits of this report. I like to thank doctoral student Juan Ortiz for his valuable support and counseling through out all this time. I would also like to express my appreciation to Jose Miguel Reynolds for his assistance with cluster support and the technical lesson provided.

To the Fusion-EP consortium, thanks for organizing the master's program, providing a platform for students to become part of the fusion community and advance in their academic careers. Through this program, I have had the privilege of meeting extraordinary professionals and fellow students. I want to extend special thanks to Peter Beyer who have been always a caring and helping mentor. I am also grateful to Rémy Guirlet, for his assistance in finding an internship and for the enriching conversations we have shared.

To the friends I made, I am deeply grateful for making my time in Marseille, Madrid and Prague a truly wonderful experience. Your presence have made a significant contribution in every aspect of my journey.

Finally, I wish to thank all my family, especially my parents and sister, who from afar have been accompany me. Their constant encouragement have been a driving force in my accomplishments. And to my cats which are a great source of motivation in difficult times.



# **Declaration in lieu of oath**

I am aware that plagiarism is not consistent with academic and research ethics. I declare in lieu of oath that all the work presented in this report, which is not cited in the text or by references, is my own work.

Madrid, Spain, the 27th of June, 2023



---

Luis Carlos Herrera Quesada

# **Copyright Agreement**

I hereby grant the FUSION-EP consortium the non-exclusive right to publish this work.

I declare that this work is free of copyright claims of third parties.

Madrid, Spain, the 27th of June, 2023



---

Luis Carlos Herrera Quesada



